

**DEVELOPMENT OF A SECOND GENERATION LINER-STYLE
HYDRAULIC SUPPRESSOR**

A Thesis
Presented to
The Academic Faculty

by

Ryan Alex Salmon

In Partial Fulfillment
of the Requirements for the Degree
Master of Science in Mechanical Engineering in the
George W. Woodruff School of Mechanical Engineering

Georgia Institute of Technology
December 2015

Copyright © 2015 by Ryan Salmon

**DEVELOPMENT OF A SECOND GENERATION LINER-STYLE
HYDRAULIC SUPPRESSOR**

Approved by:

Dr. Kenneth A. Cunefare, Advisor
Woodruff School of Mechanical Engineering
Georgia Institute of Technology

Dr. Wayne Book
Woodruff School of Mechanical Engineering
Georgia Institute of Technology

Dr. Thomas Kurfess
Woodruff School of Mechanical Engineering
Georgia Institute of Technology

Date Approved: 1 December 2015

ACKNOWLEDGEMENTS

I would like to acknowledge several people who helped me complete this work. First, I would like to thank my parents, Richard and Nadine Salmon, for their inspiration and support in both graduate school and in life. I was taught the meaning of hard work from a young age and to always persevere in difficult situations, which will inevitably arise throughout life. Thanks must be directed to my labmates René Robert, Elliott Gruber, and Ellen Skow who provided both technical help and a sense of humor when it was most needed. I would also like to thank Dr. Wayne Book and Dr. Thomas Kurfess for their participation as members of the reading committee for this work. Finally, I must thank my advisor, Dr. Kenneth Cunefare, for providing invaluable help with the research presented in this thesis, and for guiding my growth as an engineer.

TABLE OF CONTENTS

ACKNOWLEDGEMENTS	iii
LIST OF TABLES	vi
LIST OF FIGURES	vii
NOMENCLATURE	ix
SUMMARY	xii
CHAPTER 1 Introduction.....	1
CHAPTER 2 Liner Fabrication and Assembly.....	9
2.1 Liner Molds.....	9
2.2 Liner Insertion Assistive Device (LIAD)	11
2.3 Diffusor Insertion Assistive Device (DIAD)	14
2.4 Material and Cost Analysis.....	17
CHAPTER 3 Diffusor Fabrication and Analysis.....	19
3.1 Design and Finite Element Analysis (FEA)	19
3.2 Acoustic Impedance Modeling	26
3.3 Material and Cost Analysis.....	32
CHAPTER 4 Experimental Methodology	34
4.1 Experimental Setup and Transmission Loss Calculation	34
4.2 Sensor Calibration.....	41

4.3	Coherence	42
CHAPTER 5 Suppressor Transmission Loss Measurements		44
5.1	Suppressor Configuration Comparison.....	44
5.2	Suppressor Repeatability Results.....	49
5.3	Comparison Between Bladder-Style and Liner-Style Suppressors	50
CHAPTER 6 Conclusions.....		52
6.1	Future Work.....	53
Appendix A Engineering Drawings.....		55
Appendix B MATLAB Code.....		66
Appendix C Tube FEA Analysis Report		73
References.....		83

LIST OF TABLES

Table 1: Four configurations of the second generation liner-style suppressor	8
Table 2: Device prototype and final product material costs in USD.	18
Table 3: Perforate sheet relevant parameters	22
Table 4: Radial displacement parameter values.....	23
Table 5: Pressure parameter values.....	25
Table 6: Diffusor dimensions.....	28
Table 7: Hydraulic oil values	29

LIST OF FIGURES

Figure 1: Crane powered by loud hydraulics	1
Figure 2: Components of a typical bladder-style suppressor	2
Figure 3: First generation liner-style suppressor [3].....	3
Figure 4: Second generation liner-style suppressor	4
Figure 5: (a) Microspheres at atmospheric pressure and (b) post-buckling [4].....	5
Figure 6: Complete diffuser exploded view	7
Figure 7: Off-the-shelf sample of perforate sheet (unrolled).....	7
Figure 8: Liner mold comprised of the main body, end caps, and center rod	10
Figure 9: (a) The LIAD and (b) a CAD cutaway revealing interior features	12
Figure 10: Pressing operation of the liner (not shown) into the outer shell.....	13
Figure 11: (a) DIAD sections and (b) the diffuser being inserted into the liner.....	15
Figure 12: Diffuser Insertion Process	16
Figure 13: Fully assembled liner and diffuser combination	17
Figure 14: Components of the diffuser.....	20
Figure 15: Mating between shell and diffuser end caps	21
Figure 16: Assembled body and end caps (no perforate sheet)	21
Figure 17: Microscopic image of Grid0 perforate sheet [7]	22
Figure 18: Stress map of deformed tube under maximum load.....	25
Figure 19: Suppressor hydraulic circuit.....	27
Figure 20: Diffuser impedance comparison	30
Figure 21: Diffuser impedances and characteristic fluid impedance.....	30

Figure 22: Acoustic resistance of the diffusor tube and perforate sheets	32
Figure 23: The hydraulic circuit used for suppressor testing.....	35
Figure 24: Dynamic pressure sensor spacing in experimental test section.....	36
Figure 25: Upstream and downstream pressure amplitudes	37
Figure 26: The calibration block without sensors.....	42
Figure 27: Comparison of transmission loss at a system pressure of 500 psi.....	45
Figure 28: Comparison of transmission loss at a system pressure of 1000 psi.....	46
Figure 29: Comparison of transmission loss at a system pressure of 1500 psi.....	47
Figure 30: Comparison of transmission loss at a system pressure of 2000 psi.....	48
Figure 31: Repeatability test for the Grid0 configuration at 500 psi system pressure.....	50
Figure 32: Comparison between bladder-style and liner-style suppressors [16]	51
Figure 33: WM3081 suppressor outer shell drawing [19]	55
Figure 34: WM3081 suppressor end cap drawing [19]	56
Figure 35: WM3081 liner mold assembly	57
Figure 36: Liner mold bottom end cap drawing	58
Figure 37: Liner mold body drawing	59
Figure 38: Liner mold top end cap drawing.....	60
Figure 39: Liner mold center rod drawing	61
Figure 40: LIAD drawing	62
Figure 41: DIAD drawing	63
Figure 42: Diffusor tube drawing	64
Figure 43: Diffusor end cap drawing	65

NOMENCLATURE

a	Pipe inner diameter [m]
A	Cross-sectional area [m ²]
A, B, E, F	Complex wave amplitudes
c	Speed of sound [m/s]
CAD	Computer Aided Design
C_1	Constant
D	Hole perimeter [m]
DIAD	Diffusor Insertion Assistive Device
E	Young's modulus
f_0	Frequency [Hz]
FEA	Finite Element Analysis
G_{xx}	Autospectral density
G_{xy}	Cross-spectral density
h	Half plate thickness or viscous boundary layer thickness [m]
H_{ij}	Transfer function relating i and j
ID	Inner diameter [m]
k	Acoustic wavenumber [rad/m], percent open area surface factor
L	Suppressor length [m]
LIAD	Liner Insertion Assistive Device
M	Mach number

OD	Outer diameter [m]
p	System pressure [MPa]
p_{cr}	Critical buckling pressure [Mpa]
P	Percent open area
$P_{upstream}$	Upstream acoustic pressure [MPa]
$P_{downstream}$	Downstream acoustic pressure [MPa]
$Q_{upstream}$	Upstream volumetric flow [L/min]
$Q_{downstream}$	Downstream volumetric flow [L/min]
r	radius [m]
R_A	Acoustic resistance
S	Cross-sectional area [m ²]
$S_{annulus}$	Liner inner annulus surface area [m ²]
$S_{diffusor}$	Diffusor tube surface area [m ²]
t	Thickness [m]
TL	Transmission Loss
u_r	Radial displacement [m]
u_z	Axial displacement [m]
w	Hole length [m]
W_i	Incident acoustic energy [N*m]
W_t	Transmitted acoustic energy [N*m]
X_A	Acoustic reactance
Z_p	Fluid flow impedance [rayl]

Z_s	Suppressor impedance [rayl]
VI	Virtual Instrument
γ	Complex wavenumber [rad/m], ratio of specific heats
μ	Fluid viscosity [kg/m*s]
ν	Poisson's ratio
ρ	Density [kg/m ³]
σ_i	Initial radial stress [Mpa]
σ_r	Radial stress [Mpa]

SUMMARY

Noise in a fluid system can be treated with a prototypical liner-style suppressor, an expansion chamber which includes an internal annulus of syntactic foam. A syntactic foam liner consists of host material with hollow microspheres which collapse under pressure to add compliance to the suppressor. The liner effectively increases the transmission loss of the suppressor, or ratio between inlet and outlet acoustic energy. Although a first generation liner-style suppressor was developed as part of a previous study, the liner-style suppressor is not commercially available at this time. This work investigates the development of a second generation liner-style suppressor which is closer to commercialization than its predecessor.

The effect of flow-smoothing diffusors on the transmission loss of the suppressor was also investigated as part of this work. The diffusors function to constrain the liner within the device, reducing liner oscillation and the potential for turbulence-induced self-noise. The diffusor may also impact the longevity of the liner by reducing mechanical erosion. Structural and acoustic performance modeling of the prototypical diffusors was conducted in order to influence diffusor design and material selection.

Several variations of the liner-style suppressor were constructed and tested for transmission loss in an experimental test rig. The transmission loss results are indicative of suppressor acoustic performance. The acoustic performance of the suppressor configurations were compared against each other in order to determine whether an acoustically optimal configuration exists. A comparison was also made between a second generation liner-style suppressor and a similarly-sized bladder-style suppressor.

Recommendations for the development of future suppressor generations are discussed at the conclusion of the work.

CHAPTER 1

INTRODUCTION

In-line hydraulic suppressors are efficient devices used to treat noise within a fluid system. Heavy off-road construction equipment, such as the crane shown in Figure 1, utilize hydraulic systems to achieve mechanical advantage. Heavy construction equipment like the crane are capable of producing sound pressure levels up to 120 dBA [1]; high noise levels are uncomfortable for system operators and excessive structural vibrations can cause system leaks. In-line hydraulic suppressors work to reduce system fluid-borne noise, thereby decreasing the level of potentially damaging structure-borne noise and airborne noise [2].



Figure 1: Crane powered by loud hydraulics

Typical in-line suppressors consist of a cylindrical expansion chamber with a compliant internal feature used to create an impedance mismatch between end ports of the suppressor. The impedance mismatch reduces acoustic energy downstream of the suppressor. The impedance mismatch reduces acoustic energy downstream of the suppressor. Two types of in-line suppressors are known to treat noise in a fluid-system: bladder-style suppressors and liner-style suppressors.

As of the writing of this thesis, bladder-style suppressors are the only commercially available type of in-line hydraulic suppressors. A typical bladder-style suppressor is shown in Figure 2. Bladder-style suppressors utilize a bladder filled with gas to create the impedance mismatch between end ports. Although bladder-style suppressors effectively treat system noise, end-users are required to fill the internal bladder to match hydraulic system pressure. The noise control effectiveness of the bladder-style suppressor can be diminished by operator error. Furthermore, the suppressors are often located in hard-to-reach places, making it difficult to fill with gas.

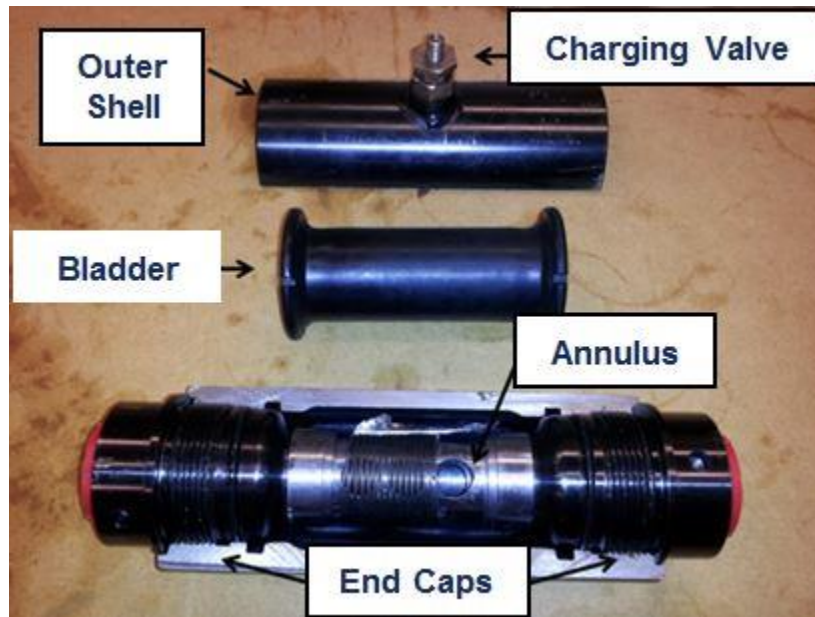


Figure 2: Components of a typical bladder-style suppressor

A better solution to the fluid system noise problem may be achieved through the use of a liner-style suppressor. The liner-style suppressor utilizes an internal annulus of compliant syntactic foam to create the impedance mismatch. A first generation liner-style suppressor, shown in Figure 3, was developed at Georgia Tech by Nicholas Earnheart [3]. The suppressor consists of a steel outer shell and the internal annulus of syntactic foam. A second generation of the liner-style suppressor was developed for the purpose of this work. The second generation device, shown in Figure 4, is closer to a commercialized, final product than the first generation device. The second generation device contains a metal diffuser which adds damping to the suppressor while also reducing turbulence-induced self-noise. The outer shell of the suppressor was supplied by Wilkes & McLean, LTD., a hydraulic accumulator and suppressor manufacturer. Dimensions of the shell provided by Wilkes & McLean can be found in Appendix A. The goal of the work presented in this thesis is to demonstrate the design, construction, and assembly of a second generation liner-style suppressor as well as to quantify the material costs and noise control performance of the device.

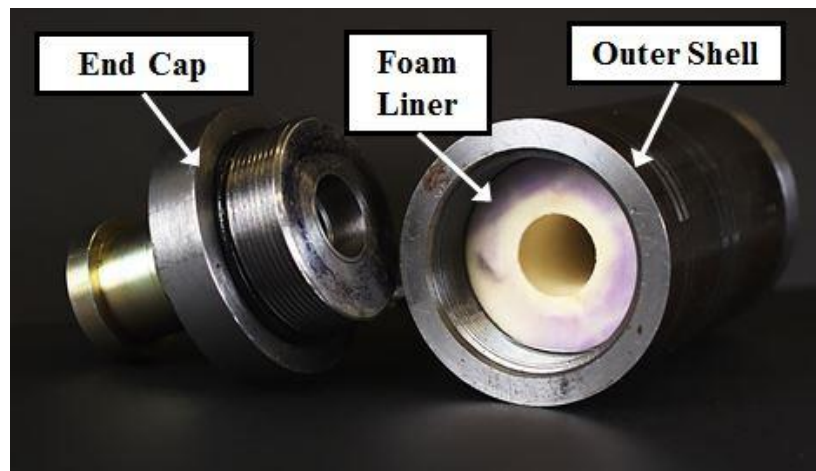


Figure 3: First generation liner-style suppressor [3]

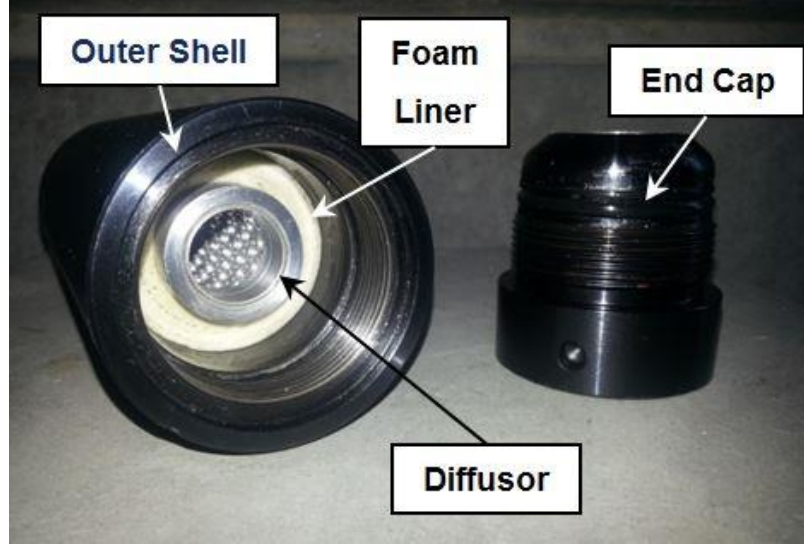


Figure 4: Second generation liner-style suppressor

The syntactic foam used for the purpose of this work, termed GR9-625, was developed at Georgia Tech by Earnhart et al. [3] for use in various fluid power noise control devices. The foam is comprised of a voided urethane host matrix identified as GR9 by its manufacturer, Goodrich Inc. Hollow microspheres manufactured by AkzoNobel fill voids in the host matrix. At atmospheric pressure the microspheres are rigid and the foam is not compliant. Figure 5 (a) shows a microscopic picture of a sample of rigid microspheres. The microspheres collapse at a critical pressure, as shown in Figure 5 (b). The critical pressure at which the microspheres collapse is given by

$$P_{cr} = \frac{2Et^2}{r^2 \sqrt{3(1-\nu^2)}}, \quad (1.1)$$

where E is the microsphere Young's modulus, ν is the microsphere Poisson's ratio, and r and t are the microsphere radius and thickness, respectively. When the system pressure in a fluid system exceeds the critical pressure, the microspheres collapse, leaving voids in

the liner host matrix. The voids are modeled as air bubbles. Because air is more compliant than the rigid microspheres, the compliance of the foam liner is increased. The compliant foam increases the impedance mismatch at the suppressor ports which leads to a reduction in the propagation of downstream acoustic energy.

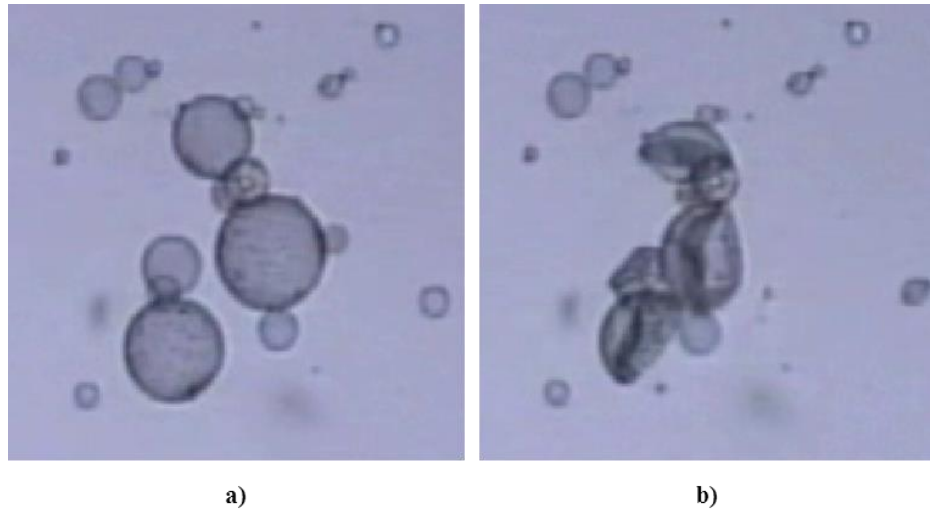


Figure 5: (a) Microspheres at atmospheric pressure and (b) post-buckling [4]

Custom-fabricated aluminum diffusors serve several functions: increase damping in the suppressor, decrease turbulence-induced self-noise of the suppressor, and reduce the potential for microsphere shedding into the system, which can create leaks and damage system components. The diffusor counteracts radial and axial displacement of the liner at elevated hydrostatic pressure. The liner experiences radial and axial displacement according to

$$u_r = -\frac{P}{E_L}(1-\nu_L)r, \quad (1.2)$$

and

$$u_z = -\frac{p}{E_L}(1-2\nu_L)z, \quad (1.3)$$

where p is the system pressure, E_L is the bulk modulus of the liner, ν_L is the Poisson's ratio of the liner, r is the radial coordinate, and z is the axial coordinate [3]. The above equations show that the liner ID and overall length shrink as hydrostatic pressure is increased. At elevated hydrostatic pressure, the decrease in liner length causes the liner to fall out of position in the suppressor shell; the liner is no longer constrained and pressure fluctuations in the flow cause the liner to oscillate in the shell. The oscillations, which contribute to the suppressor self-noise, are eliminated by connecting the liner to a fully constrained diffusor.

The complete diffusor is comprised of four parts: the main body (or "tube"), two end caps, and a microperforate sheet which wraps around the main body like an outer sleeve. Figure 6 shows an exploded CAD view of the diffusor components. The perforate sheet has thousands of microscopic holes (not shown in Figure 6) which add damping to the suppressor. A unrolled sample of one of the perforate sheets used in this study is shown in Figure 7; the numerous microscopic holes can be seen in the figure. The introduction of damping by the perforate sheet serves to increase the noise reduction performance of the suppressor. While the liner adds significant compliance to the system, it adds an insignificant amount of damping. Both compliance and damping in the suppressor affect suppressor impedance, which in turn affects the noise reduction performance of the suppressor. The perforate sheet also reduces direct impingement of hydraulic oil on the liner's inner annulus. It is expected that prolonged, direct exposure to hydraulic oil will cause the liner to shed microspheres into the fluid system. Microspheres

have the potential to damage seals and pumps in the system. It is important to note that the perforate sheet does not act as a filter of the microspheres; collapsed microsphere diameters are smaller than the perforate's hole diameters. Rather, the sheet behaves like a protective covering, reducing shear stress on the liner's inner annulus. Two types of perforate sheets were modeled and tested for the purpose of this work. The sheets were designated with the names Grid0 and Grid1.

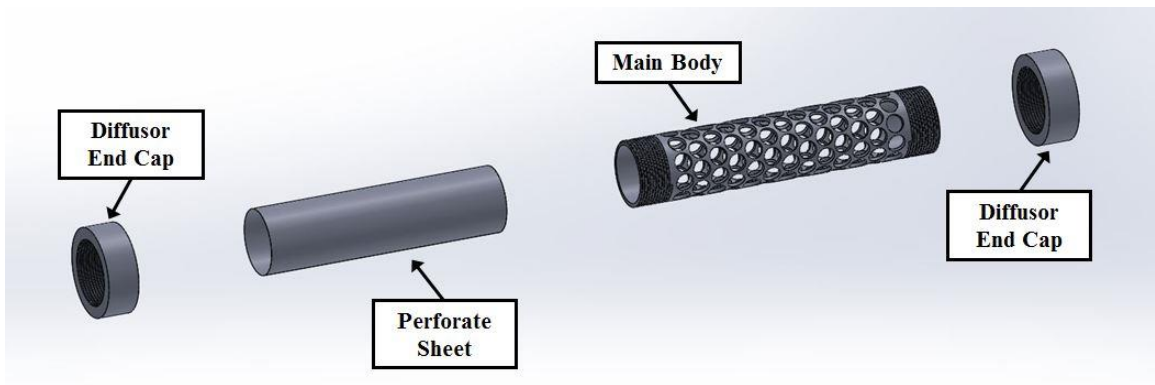


Figure 6: Complete diffuser exploded view

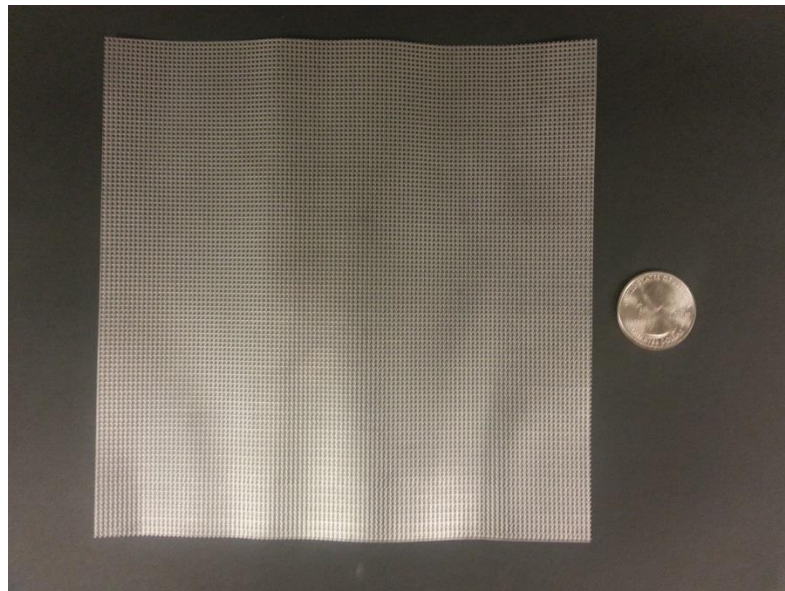


Figure 7: Off-the-shelf sample of perforate sheet (unrolled)

Four variations of the second generation liner-style suppressor were tested to measure acoustic performance. The configurations are listed in Table 1. The performance of a suppressor is measured by its transmission loss, the ratio between inlet and outlet acoustic energy. The transmission loss, which is frequency dependent, is measured with a test rig that is comprised of a hydraulic circuit and associated measurement instrumentation.

Table 1: Four configurations of the second generation liner-style suppressor

Configuration	Components
1	Outer Shell; Liner
2	Outer Shell; Liner; Diffusor Main Body
3	Outer Shell; Liner; Diffusor Main Body; Grid0
4	Outer Shell; Liner; Diffusor Main Body; Grid1

The following sections of this work will discuss the fabrication and assembly of the second generation liner-style suppressor, analyses conducted on suppressor components, experimental methodology, the acoustic performance of each suppressor configuration, and recommendations for future development of a commercialized liner-style suppressor. The liner molds and insertion devices are discussed in Chapter 2. Chapter 3 discusses diffusor fabrication, structural analysis, and performance models. Chapter 4 describes the experimental methodology used to obtain suppressor transmission loss measurements. Test results, discussed in Chapter 5, provide further insight as to the optimal second generation liner-style suppressor configuration. Chapter 6 concludes the work and presents a discussion on the future of liner-style suppressors.

CHAPTER 2

LINER FABRICATION AND ASSEMBLY

A major motivation of this work was the development of a fabrication and assembly methodology used to construct a second generation liner-style suppressor. A prototypical liner mold and a liner insertion assistive device (LIAD) were designed to fabricate and insert the syntactic foam liners into the suppressor outer metal shell. The diffusor insertion assistive device (DIAD) was designed to insert the diffusor into the liner, which can then be inserted into the outer shell. Sections 2.1-2.3 discuss design and construction constraints, as well as assembly processes associated with the various components. Two-dimensional engineering drawings of each device are found in Appendix A. Chapter 2 will finish with a high-level cost analysis of the liner fabrication and assembly process.

2.1 Liner Molds

A prototypical liner mold was custom-machined in order to cast the syntactic foam liners used in the second generation suppressors. The mold, shown in Figure 8, was fabricated at Georgia Tech and sent to UTAS in Jacksonville, Florida for casting of the liners.

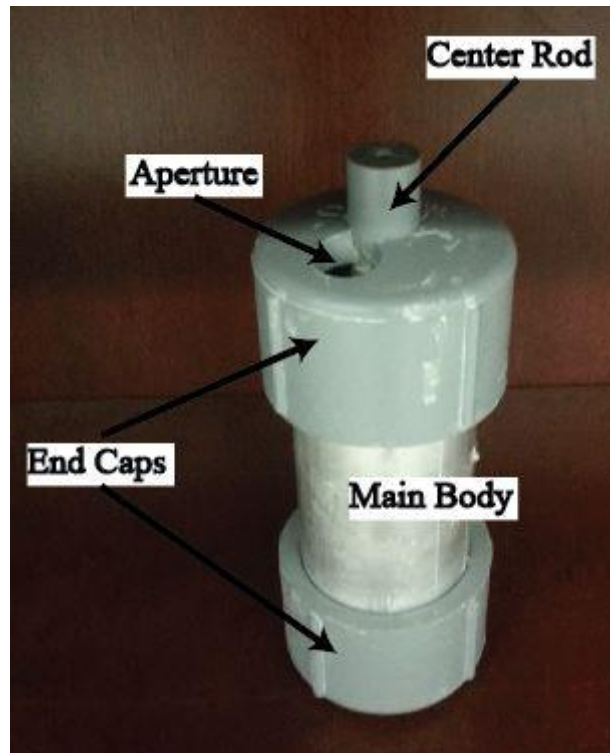


Figure 8: Liner mold comprised of the main body, end caps, and center rod

Four parts make up the complete mold: an aluminum body, CPVC center rod, and two CPVC end caps. CPVC was chosen for several parts as it is inexpensive, easily machinable, and rated for temperatures as high as 93°C [5]. The high temperature rating of CPVC is important because the casting process occurs at a maximum temperature of about 70°C [6]. Although cheaper, and more readily accessible, PVC parts were not chosen for the mold as their maximum temperature rating is 60°C [5]. The CPVC end caps and center rod were purchased off-the-shelf and required very little machining. The end caps allow for the rod to be centered in the mold; the rod displaces the GR9-625 mixture during casting, thus creating the inner annulus of the liner. A small aperture in the top cap allows for pouring of the syntactic foam mixture prior to casting. An

aluminum alloy was chosen for the mold body as it has a smooth interior surface finish which allows for ease of demolding of the liner from the mold.

Several constraints influenced the design of the prototypical liner mold. The mold is required to be six inches or less in length in order to fit inside the casting oven at UTAS. Another design constraint involved creation of the annular hole. The final mold prototype has the hole cast initially as opposed to earlier mold versions which lacked a center rod and had the hole bored out with a twist bit drill, during post-processing. The drilling operation causes the liner's inner annulus to have a rough finish, which encourages turbulent flow and self-induced flow noise. The mold body ID was purposefully oversized to accommodate for liner shrinkage during the casting process. It is estimated that the liner shrinks about 0.008% during casting [6]. It is important to note that the prototypical mold is suitable for casting of the liners at a small scale, but large scale manufacturing of a liner-style suppressor would require a more efficient liner casting method.

2.2 Liner Insertion Assistive Device (LIAD)

The liner insertion assistive device, or LIAD, guides the liner as it is inserted into the steel outer shell. Figure 9 shows a picture of the LIAD and a CAD cutaway of its interior. The LIAD serves two functions: compress the liner to fit inside the shell and protect the liner from being damaged by the internal threads at the shell entrance. The uncompressed liner was designed to fit flush with the shell center interior diameter (See Appendix A). However, the liner must first be compressed at the smaller diameter ports before it can reach the center of the shell where it returns to its uncompressed state; the

LIAD assists with the compression process into the ports by guiding the uncompressed liner through a smooth gradient, like a funnel. The lower body of the LIAD was extended in order to protect the liner from the metal shell's internal threads, which would easily shred the outer surface of the liner, releasing microspheres into the system. Although there have not been any studies to date conducted on the impact of shredded microspheres into a fluid system, it is believed that loose microspheres in the system put system components at risk.

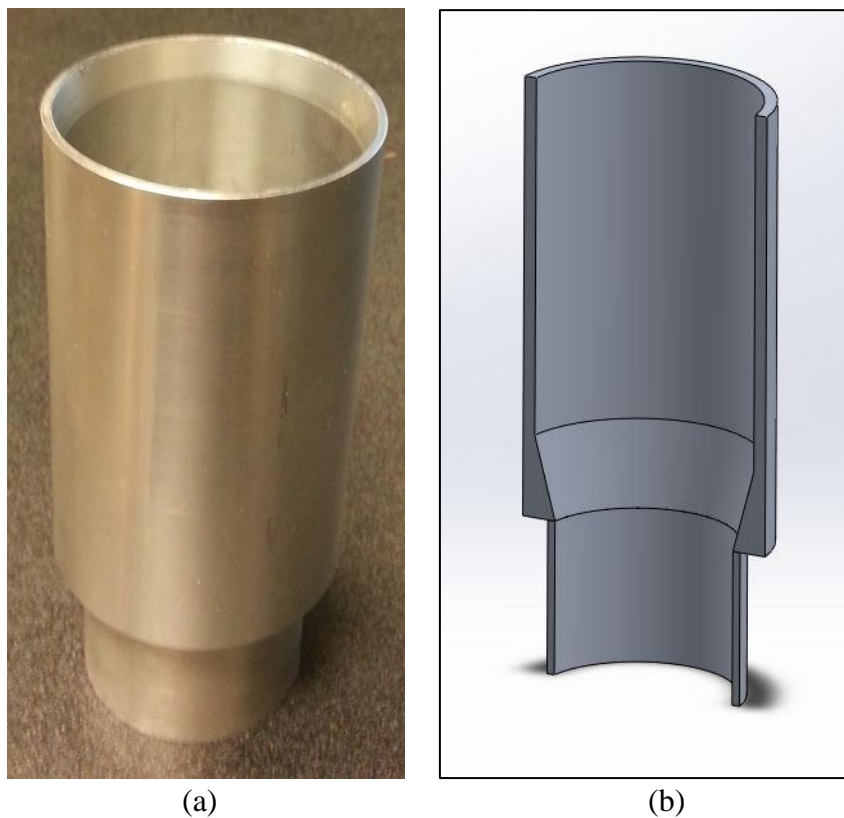


Figure 9: (a) The LIAD and (b) a CAD cutaway revealing interior features

A mechanical press, or arbor, provides the leverage needed to compress the liner through the LIAD. Figure 10 shows a snapshot of the liner insertion assembly process. A white, cylindrical pushing block drives the liner through the LIAD. The pushing block

was fabricated in order to increase the effective surface area of the rectangular ram on the arbor. Without the pushing block, the narrow ram causes the liner to “mushroom” upwards and around the ram. Excessive force on the liner surface without the block causes irreversible damage of the liner. The liner, LIAD, and metal shell were lubricated with a thin film of synthetic grease to ease the pressing operation.

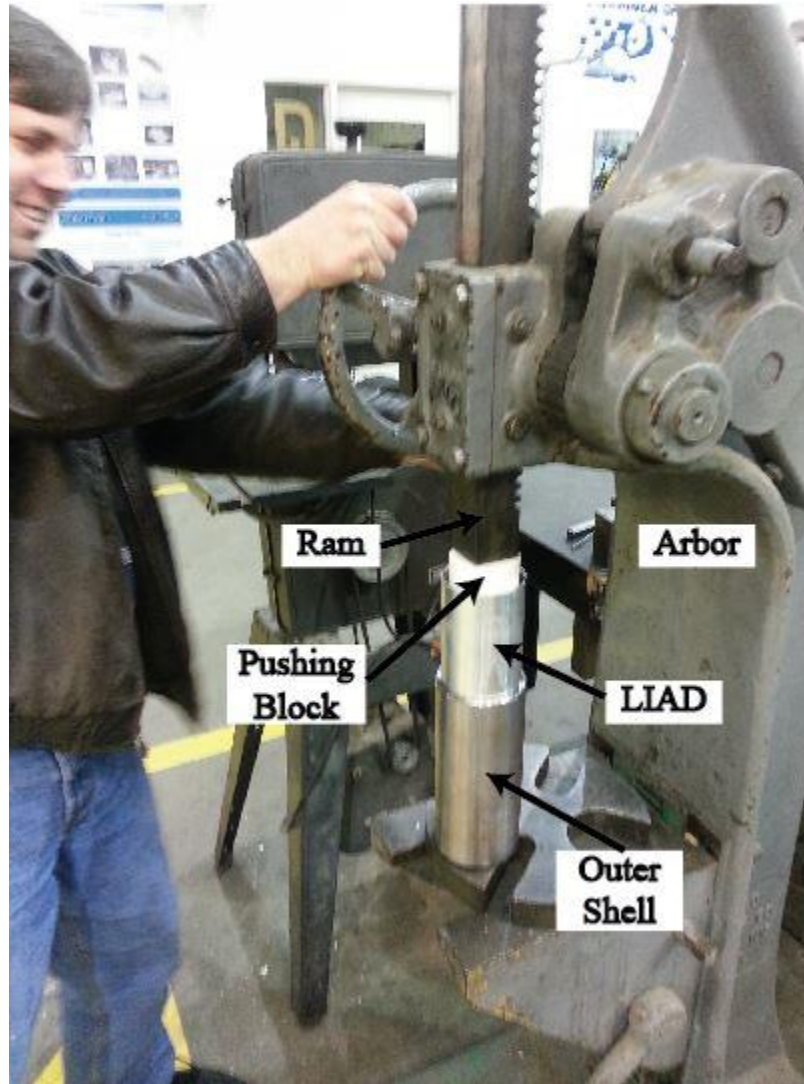
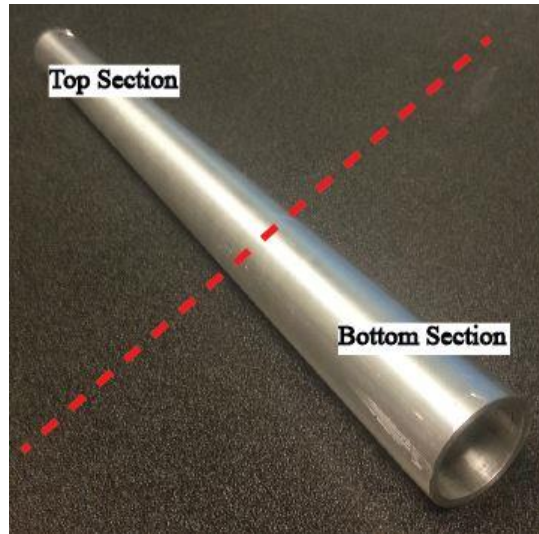


Figure 10: Pressing operation of the liner (not shown) into the outer shell

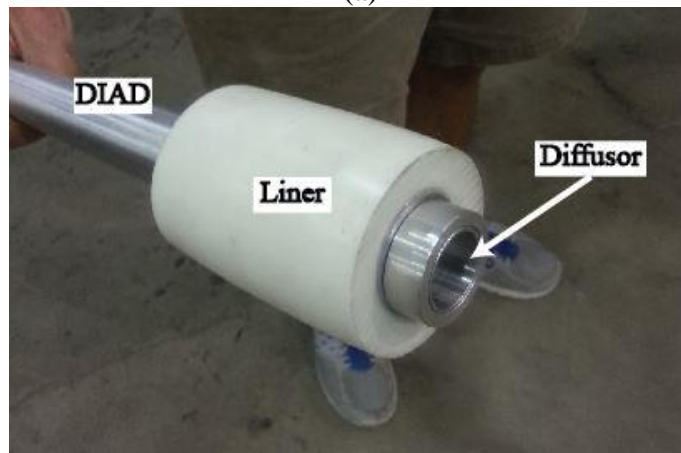
The LIAD was designed to accommodate the insertion of either the liner or the liner and diffuser combination. However, before a liner and diffuser combination can be inserted into the shell, the diffuser must be inserted into the liner. Another device, called the diffuser insertion assistive device (DIAD) was constructed in order to assemble the liner and diffuser combination. The DIAD is discussed in further detail in the following section.

2.3 Diffuser Insertion Assistive Device (DIAD)

The DIAD temporarily increases the ID of the liner in order to accommodate diffuser insertion. Figure 11 (a) shows an isometric view of the DIAD and Figure 11 (b) shows an assembly step where the diffuser is being inserted into the liner. In order to better explain the assembly process, the DIAD is assigned a top section and a bottom section. The top and bottom sections are separated by the transverse axis of the DIAD which cuts through the geometric center of the device. A red dashed line separates the sections in Figure 11 (a). The bottom section of the DIAD contains the larger diameter aperture used to stretch the liner ID while also holding the diffuser in place during assembly. The bottom section of the DIAD is shown in the bottom-right corner of Figure 11 (a); the bottom section is also shown in Figure 11 (b). The top section of the DIAD fits snugly into the inner annulus of the uncompressed liner. The top section of the DIAD is shown in the top-left corner of Figure 11 (a).



(a)



(b)

Figure 11: (a) DIAD sections and (b) the diffusor being inserted into the liner

Several steps need to be followed when inserting the diffusor into the liner. To begin, the DIAD is placed vertically on the base of the mechanical press; the bottom section of the DIAD should be touching the base of the press. The entire body of the DIAD is then coated with synthetic grease to ease the insertion process. The next step is to place the uncompressed liner on the top section of the DIAD. A hollow pushing cylinder, shown in Figure 12, is placed on top of the liner. The cylinder is a necessary assembly device – without it, the solid ram of the mechanical press interferes with the

DIAD. The cylinder essentially increases the pressing range of the ram. The liner is pushed down the body of the DIAD until it reaches the arbor base.

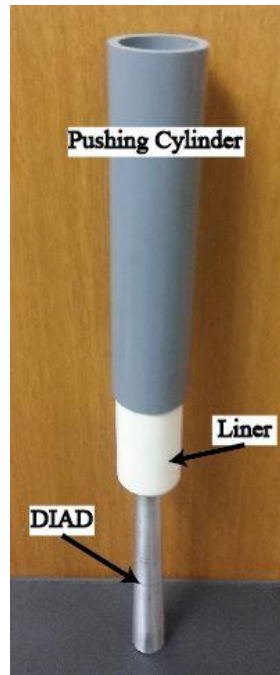


Figure 12: Diffusor Insertion Process

The DIAD, liner, and cylinder are now turned 180° vertically. The diffusor is inserted into the opening of the DIAD. The DIAD, liner, and diffusor combination rests on the pushing cylinder which is now touching the arbor base. A slender rod (not shown) was fabricated to fit inside the ID of the diffusor. The top of the rod interfaces with the arbor ram and the bottom of the rod interfaces with the floor of the DIAD opening. The rod is used to slowly push the DIAD through the pushing cylinder towards the floor; the DIAD moves through the liner's inner annulus and the liner ID locks onto the diffusor. The fully assembled liner and diffusor configuration is shown in Figure 13, with a quarter pictured for scale.



Figure 13: Fully assembled liner and diffuser combination

2.4 Material and Cost Analysis

The liner mold, LIAD, and DIAD are relatively inexpensive and robust devices that can be reused for small scale production of second generation liner-style suppressors. Table 2 outlines the material cost of the three devices. The prototypes of these devices are made of CPVC and aluminum alloy. Although these materials are cost-effective and easy to machine, final products would likely be constructed out of stainless steel or a related steel alloy. The number and complexity of the parts is low enough to warrant final products constructed of steel, which is more robust than aluminum. The table also provides a total cost estimate for the final product devices.

Table 2: Device prototype and final product material costs in USD.

Device	Material Cost [8]	Total Cost
Mold Prototype	61.11	136.94
LIAD Prototype	39.74	
DIAD Prototype	36.09	
Mold Final Product	82.45	188.03
LIAD Final Product	41.77	
DIAD Final Product	63.81	

CHAPTER 3

DIFFUSOR FABRICATION AND ANALYSIS

Diffusor design, structural strength, acoustic performance modeling, and manufacturability are discussed in detail in this chapter. Section 3.1 focuses on diffusor main body (or “tube”) design constraints and a static load FEA analysis of the tube. Acoustic impedance modeling of the diffusor tube and perforate sheets is explored in section 3.2. The impedance modeling was used to influence tube design and perforate sheet selection. Section 3.3 discusses material selection and fabrication costs associated with the diffusor.

3.1 Design and Finite Element Analysis (FEA)

A diffusor body, two end caps, and perforate sheet constitute the complete diffusor, as shown in Figure 14. The diffusor body is a thin tube made of 6061 aluminum alloy. The surface of the tube contains 130 holes, each measuring 1/4” in diameter. Initially, the number and size of the holes were chosen arbitrarily. The only geometric design constraint was that the tube could not collapse under the predicted maximum load, which is expected to occur during the insertion of the liner and diffusor into the suppressor shell. An FEA, described later in the section, was conducted on the proposed tube design to ensure the device had adequate structural integrity.

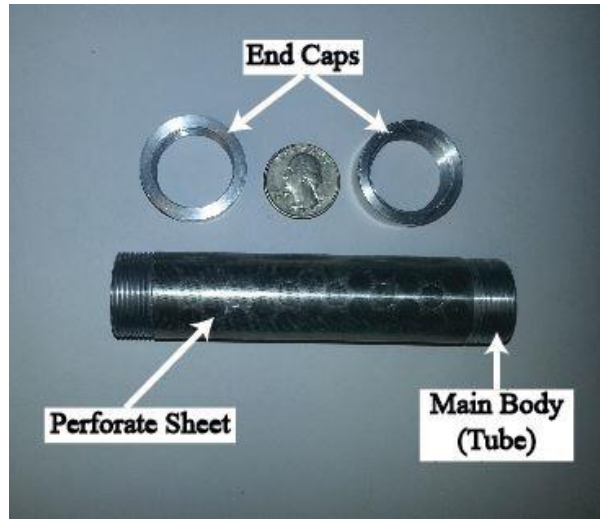


Figure 14: Components of the diffuser

Two identical end caps made of 6061 aluminum screw onto the ends of the tube. The symmetry of the diffuser body allows for fabrication of a singular end cap part that can fit on either side of the body – this is especially important for proposed large-scale manufacturing of the diffuser where simple part fabrication and device assembly can save time and money. The diffuser end caps fit flush inside the counterbore of the outer shell end caps as illustrated by Figure 15. Mating between the shell end caps and diffuser end caps constrains the diffuser within the suppressor, one of the primary diffuser functions mentioned in Chapter 1. The diffuser end caps were designed with the ability to detach from the tube in order to allow for ease of assembly into the liner via the DIAD. At least one of the diffuser caps needs to be unscrewed for insertion into the DIAD. After the insertion process is complete, both end caps are screwed onto the diffuser for insertion into the suppressor shell via the LIAD. Figure 16 shows a diffuser tube with both end caps screwed on. Detailed two-dimensional engineering drawings of the diffuser body and end caps can be found in Appendix A.



Figure 15: Mating between shell and diffuser end caps

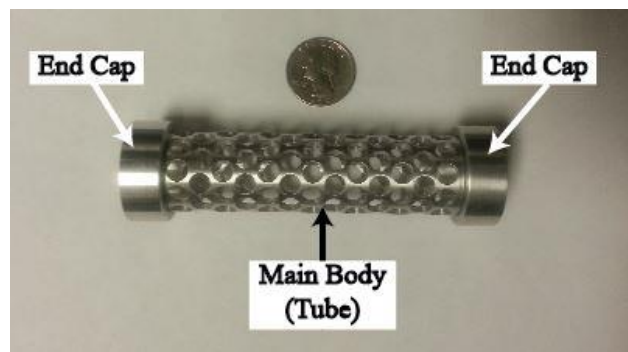


Figure 16: Assembled body and end caps (no perforate sheet)

Two different perforate sheets were examined as part of the work. The first sheet, referred to as Grid0, was previously purchased and the manufacturer is unknown. Sheet specifications such as hole size and percent open area were determined upon examination of an image taken by a microscope. Figure 17 shows the Grid0 microscope image. The second perforate sheet, referred to as Grid1, is supplied by McMaster Carr. The sheet was chosen based on sample availability and an analysis of its resistivity, to be further discussed in the next section. Table 3 compares various sheet parameters of importance to

the thesis. A microscopic image of Grid1 was not examined as relevant parameters were found online.

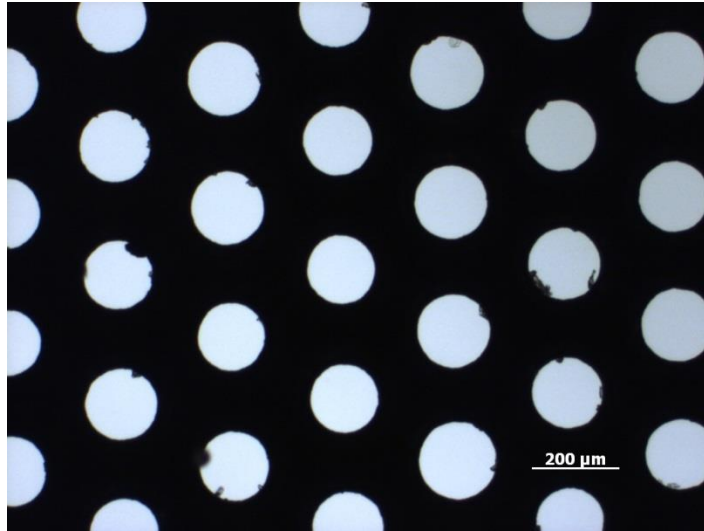


Figure 17: Microscopic image of Grid0 perforate sheet [7]

Table 3: Perforate sheet relevant parameters

Parameter	Grid0	Grid1
Hole Diameter	1.60×10^{-4} [m]	5.08×10^{-4} [m]
Open Area	27%	22%
Thickness	1.20×10^{-4} [m]	2.03×10^{-4} [m]

A structural analysis was performed on the diffuser main body using the simulation package in SolidWorks. A critical part of the analysis was the calculation of the maximum distributed pressure on the diffuser surface. It is assumed that the diffuser experiences maximum loading during insertion through the LIAD into the outer shell of the suppressor. The pressure on the diffuser is equal and opposite to the radial stress experienced by the liner annulus during compression. Liner annulus radial stress is given by

$$\sigma_r = \frac{E}{1-\nu^2} \left[C_1(1+\nu) - C_2 \frac{1-\nu}{r^2} \right], \quad (3.1)$$

where E is the liner Young's modulus, ν is the liner Poisson's ratio, r is the radial distance from the center of the liner to the liner ID, and C_1 and C_2 are constants determined by boundary conditions at the liner ID and OD [3]. The constants C_1 and C_2 are determined through solution of

$$u_r = C_1 r + \frac{C_2}{r}, \quad (3.2)$$

where u_r is the liner displacement and r is the radial coordinate where displacement occurs. A system of equations was developed using known displacements at the two boundary conditions. The system of equations is rearranged into matrix form in Equation (3.3),

$$\begin{bmatrix} r_{OD} & \frac{1}{r_{OD}} \\ r_{ID} & \frac{1}{r_{ID}} \end{bmatrix} \begin{bmatrix} C_1 \\ C_2 \end{bmatrix} = \begin{bmatrix} u_{r,OD} \\ u_{r,ID} \end{bmatrix}. \quad (3.3)$$

Table 4 lists parameter values associated with Equation (3.3).

Table 4: Radial displacement parameter values

Parameter	Value [units]
r_{ID}	2.03×10^{-2} [m]; 0.920 [in]
r_{OD}	4.40×10^{-2} [m]; 1.75 [in]
$u_{r,ID}$	2.70×10^{-2} [m]; 0.108 [in]
$u_{r,OD}$	7.90×10^{-2} [m]; 0.312 [in]
C_1	2.00×10^{-1} [m]; 7.87 [in]
C_2	-4.50×10^{-5} [m]; -0.002 [in]

An iterative code was developed in order to determine the radial stress according to Equation (3.1). An iterative process is necessary because material properties of the liner vary with stress, which is unknown. The code is included in Appendix B. The code initially sets the radial stress, σ_i , to 0. Then, the radial stress σ_{i+1} is calculated using E and ν values at a pressure of zero MPa. The difference between σ_{i+1} and σ_i is calculated and checked against a preset tolerance. If the difference is greater than the tolerance, the next radial stress, σ_{i+2} , is calculated using E and ν values of the liner under increased pressure. This process is repeated until the difference between consecutive radial stress values is less than the tolerance. Once the difference is within the tolerance, the stress has converged and the code is terminated. The pressure on the diffuser tube surface was then calculated using

$$p = k\sigma_r, \quad (3.4)$$

where p is the pressure, and k is the percent open area surface factor. The percent open area surface factor was determined by

$$k = \frac{S_{annulus}}{S_{diffusor}}, \quad (3.5)$$

where $S_{annulus}$ is the surface area of the liner inner annulus and $S_{diffusor}$ is the surface area of the diffuser tube. Table 5 lists parameter values from Equation (3.4) and Equation (3.5). Figure 18 shows the result of the SolidWorks FEA static load simulator using the calculated pressure value and a high quality solid mesh.

Table 5: Pressure parameter values

Parameter	Value [units]
$S_{annulus}$	1.23×10^{-2} [m ²]; 19.0 [in ²]
$S_{diffusor}$	2.08×10^{-3} [m ²]; 3.23 [in ²]
k	5.89
σ_r	3.35 [MPa]
p	19.7 [MPa]

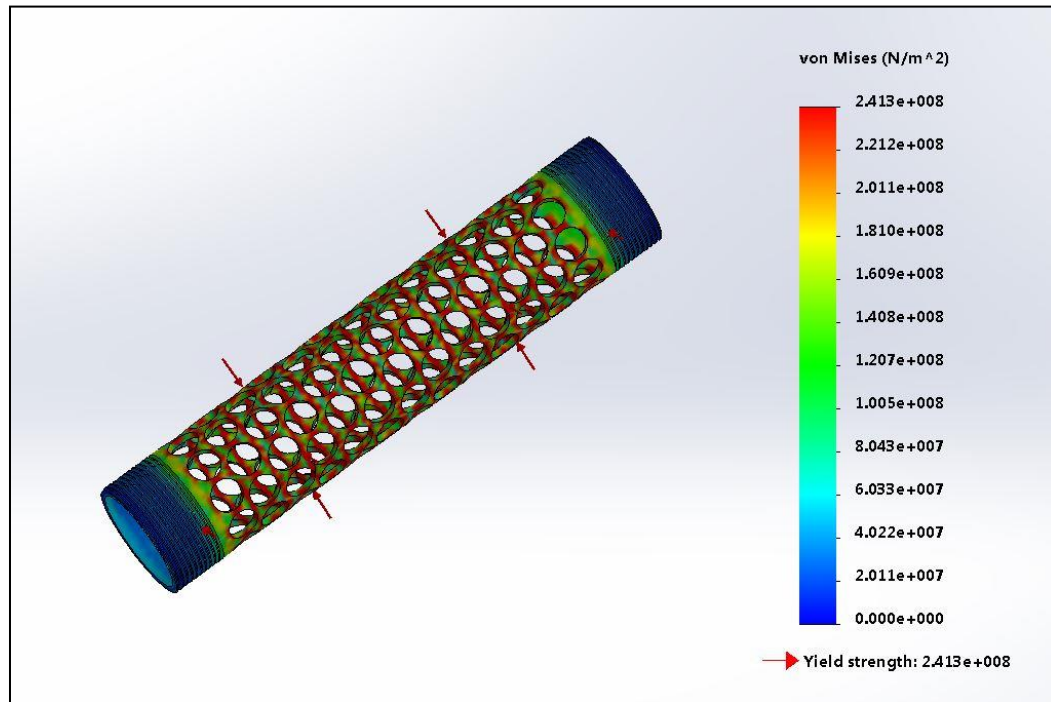


Figure 18: Stress map of deformed tube under maximum load

Red-colored areas in Figure 18 show where yielding occurs under load. Spots of red cover the tube surface near the holes. It is important to note that although yielding occurs near the holes, the resulting deformation from the yielding is not predicted to be significant. Deformations are on the order of microns, as illustrated by a full simulation

report in Appendix C. Because the simulation shows that the tube body does not collapse under maximum expected load, the design of the tube was considered to be suitable.

3.2 Acoustic Impedance Modeling

An impedance model of the diffuser tube and perforate sheets was developed in order to predict the acoustic performance of different suppressor configurations. Three of the suppressor configurations listed in Chapter 1 utilize some form of the diffuser. Configuration 2 utilizes the diffuser tube, while configuration 3 and configuration 4 utilize either a combination of the tube and Grid0, or the tube and Grid1, respectively. A hydraulic circuit of the suppressor is shown in Figure 19. The circuit shows the suppressor impedance, Z_s , in parallel to the fluid flow impedance, Z_p . Here, the impedances are modeled in parallel because upstream acoustic energy that reaches the suppressor is either dissipated through the suppressor or propagated downstream. The majority of the upstream volumetric flow, Q_{in} , travels along the path with the lowest impedance. If Z_s is designed to be much less than Z_p , then Q_1 will be much greater than Q_2 and acoustic signals will penetrate the diffuser into the liner.

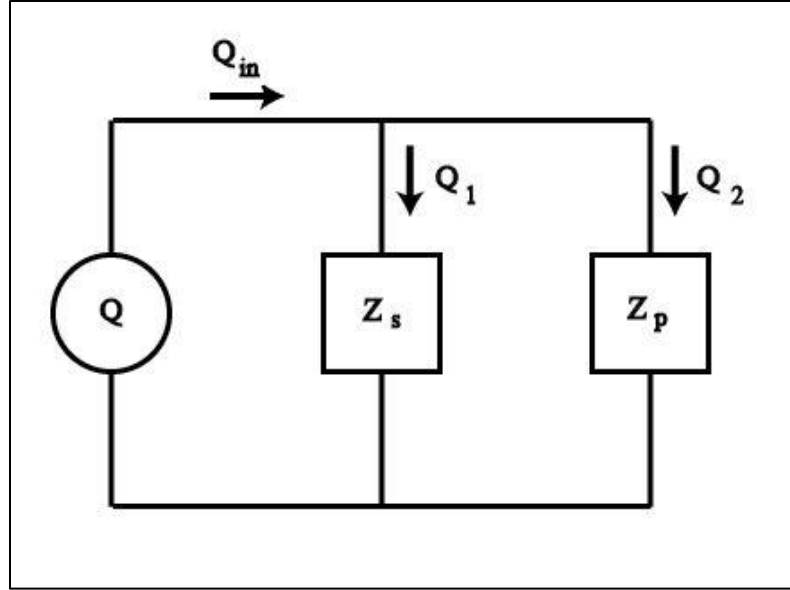


Figure 19: Suppressor hydraulic circuit

The specific acoustic impedance for flow through a pipe is

$$Z_p = \frac{\rho c}{A}, \quad (3.6)$$

where ρ is the density of ISO 46 hydraulic oil, c is the speed of sound in hydraulic oil, and A is the cross-sectional area of the pipe [8].

The impedance of each suppressor is a function of its diffusor impedance. When designing the diffusor, its impedance should be as small as possible to encourage good communication of acoustic signals through the suppressor. Diffusor impedance, Z_s , was calculated using

$$Z_s = \frac{100}{PS} (j\rho \tan(kl(1-M)) + R_A A), \quad (3.7)$$

where P is percent open area, S is the perforate area, ρ is the density of the hydraulic oil,

k is the acoustic wavenumber, M is the Mach number, R_A is the acoustic resistance, and A is the area of a single hole in S [9]. The acoustic resistance, R_A , was calculated using

$$R_A = \frac{\rho c}{A} \left[\frac{ktDw}{2A} \left[1 + (\gamma - 1) \sqrt{\frac{5}{3\gamma}} \right] + 0.288kt \log \left[\frac{4A}{\pi h^2} \right] + \varepsilon \frac{Ak^2}{2\pi} + M \right], \quad (3.8)$$

where D is the perimeter of a hole in either the tube or perforate sheet, w is the length of a hole, k is the acoustic wavenumber, and γ is the ratio of specific heats for the working fluid [9]. In the previous equation, t is the viscous boundary layer, defined by

$$t = \sqrt{\frac{2\mu}{\rho\omega}}, \quad (3.9)$$

where μ is the fluid viscosity, ρ is the fluid density, and ω is the acoustic frequency [9]. The parameter h is either the half plate thickness or the viscous boundary layer, whichever is larger [9]. Table 6 shows values of the various diffuser dimensions used in the code. Table 7 shows fluid property values used in the code.

Table 6: Diffuser dimensions

Parameter	Tube	Grid0	Grid1
P	62%	27%	22%
S	6.60×10^{-3} [m]	6.60×10^{-3} [m]	6.60×10^{-3} [m]
l	2.70×10^{-3} [m]	1.20×10^{-4} [m]	2.03×10^{-4} [m]
A	3.17×10^{-5} [m]	2.01×10^{-8} [m]	2.03×10^{-7} [m]
D	1.20×10^{-2} [m]	5.03×10^{-4} [m]	1.60×10^{-3} [m]
ϵ	0	0	0

Table 7: Hydraulic oil values

Parameter	ISO 46 Hydraulic Oil
ρ	861 [kg/m ³]
c	1400 [m/s]
μ	3.96x10 ⁻² [kg/ms]
γ	1
M	0

Bies and Hanson et al. recommend setting the parameter ε to zero for radiation into spaces of diameter much less than a wavelength of sound [9]. The ratio of specific heats, γ , is equal to 1 for fluids. The Mach number, M , of the fluid flow is approximately equal to zero for sound speeds measured in the circuit. Using these parameter values, Equation (3.7) and Equation (3.8) can be reduced to

$$Z_s = \frac{100}{PS} (j\rho \tan kl + R_A A), \quad (3.10)$$

and

$$R_A = \frac{\rho c}{A} \left[\frac{ktDw}{2A} + 0.288kt \log \left[\frac{4A}{\pi h^2} \right] \right]. \quad (3.11)$$

If a diffusor is constructed of both the tube and a perforate sheet, its impedance is calculated as a series combination of the tube impedance and the sheet impedance. A MATLAB code, presented in the Appendix, was developed to calculate diffusor impedances. Figure 21 compares the various diffusor impedances to Z_p . The size and number of holes on the diffusor tube and perforate sheets were designed such that the total impedance of the diffusor is much less than Z_p . Total impedances of the diffusors

are about three orders of magnitude less than the characteristic impedance of the fluid and acoustic signals will successfully penetrate to the liner.

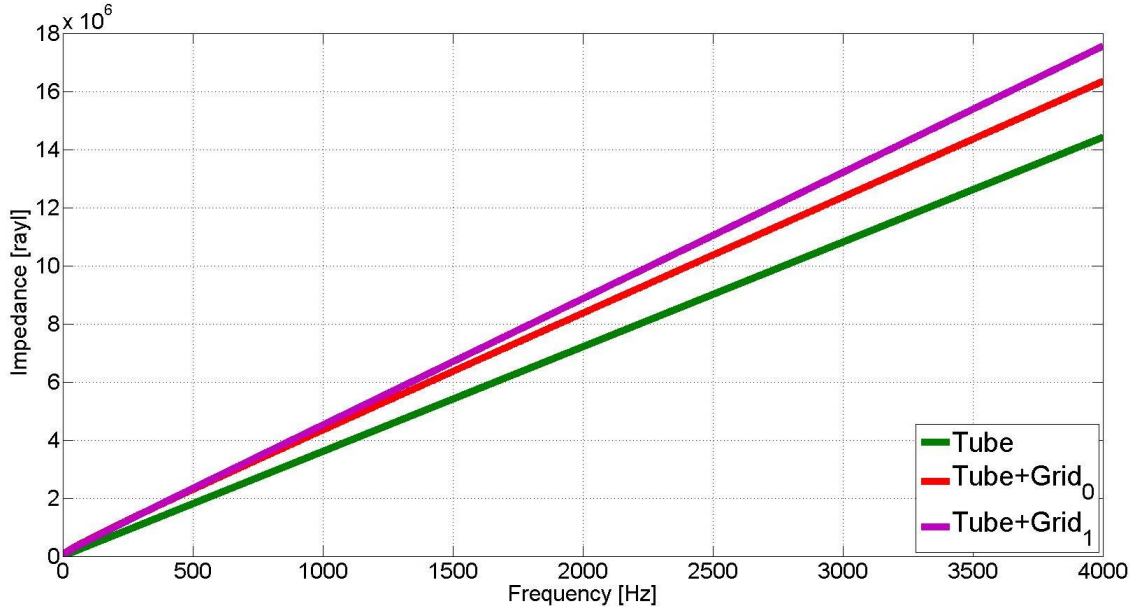


Figure 20: Diffusor impedance comparison

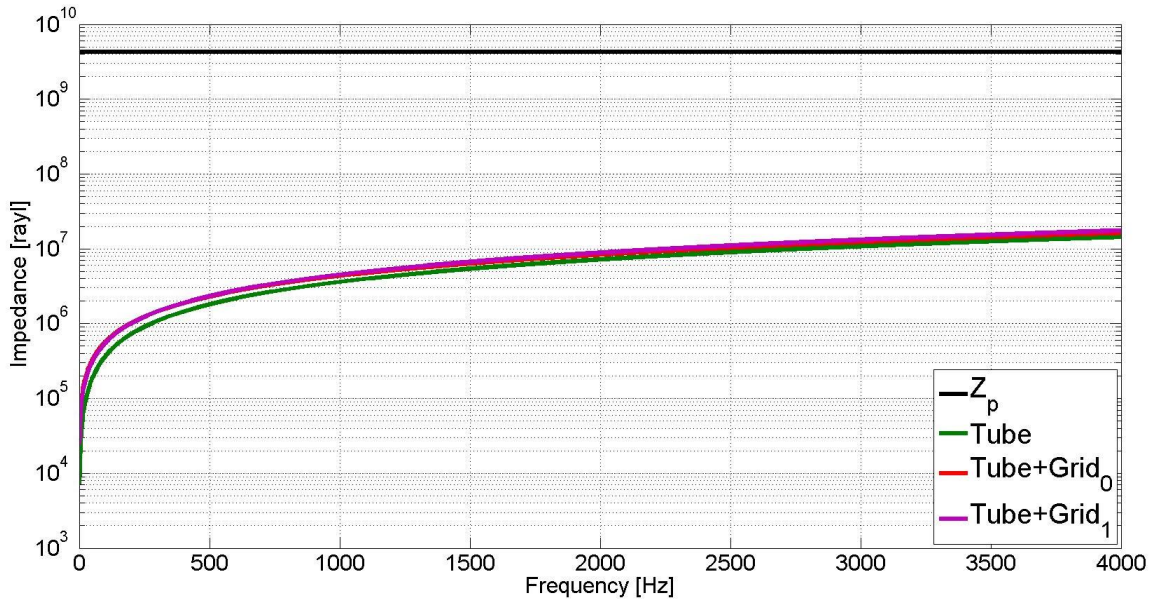


Figure 21: Diffusor impedances and characteristic fluid impedance

Equation (3.10) can be rewritten as the complex combination of a real part and an imaginary part

$$Z_S = R_A + jX_A, \quad (3.12)$$

where the real part, R_A , is the acoustic resistance and the imaginary part, X_A , is the acoustic reactance. The real part of Equation (3.12) influenced the perforate sheet selection process. As discussed in Chapter 1, the small holes of the perforate sheet are intended to break up fluid flow, adding resistivity and damping to the diffusor [9]. The added resistivity corresponds to an increase in R_A . High resistivity corresponds to an acoustically rigid system, while low resistivity corresponds to an acoustically flexible system - neither of which will benefit acoustic performance; optimal resistivity lies somewhere in the middle, but is not precisely known at the time of this work. The resistivity of the Grid0 diffusor, Grid1 diffusor, and the diffusor tube was examined using the MATLAB code in Appendix B. The results of the analysis are shown in Figure 22.

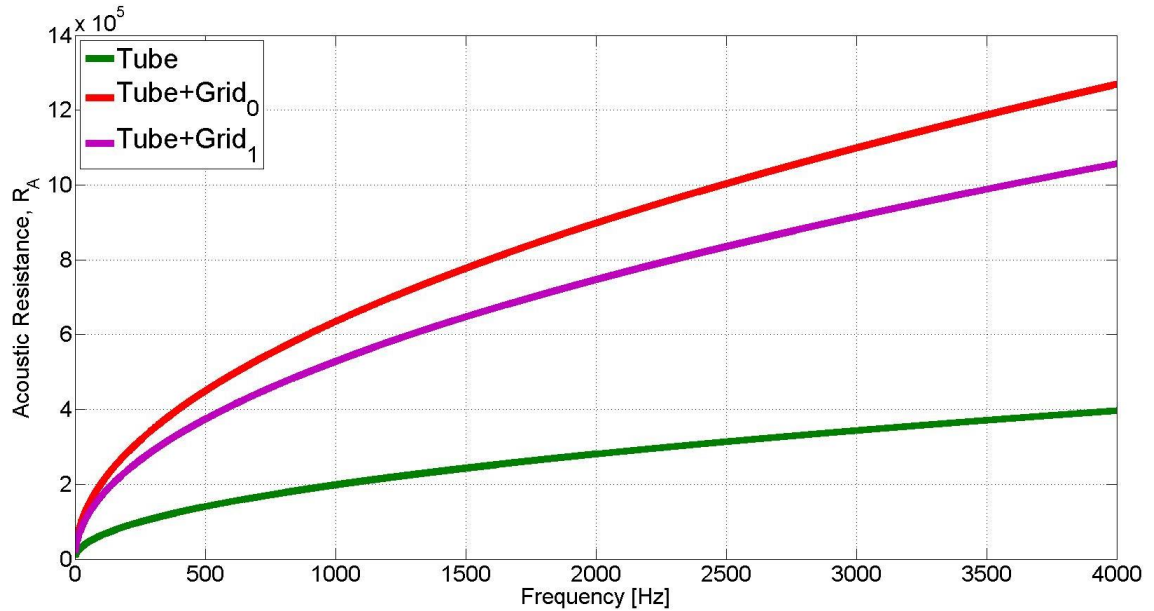


Figure 22: Acoustic resistance of the diffuser tube and perforate sheets

The Grid0 diffuser shows the highest resistivity across the modeled frequency spectrum, while the diffuser tube shows the lowest resistivity. The Grid1 diffuser shows a relatively moderate resistivity compared to the other configurations. It was hypothesized that the moderate resistivity of the Grid1 diffuser would result in improved suppressor acoustic performance. The acoustic resistance of the sheets and their correlation to suppressor transmission loss results is discussed in Chapter 5.

3.3 Material and Cost Analysis

The prototypical diffuser tubes used in this research were constructed using 6061 aluminum alloy. The cost to produce each prototypical diffuser (including perforate sheet) was \$10.38, excluding any labor costs [10]. Aluminum alloy is relatively inexpensive and easy to machine, desirable traits for initial prototypes. The FEA

discussed in section 3.1 showed that an aluminum diffuser will not fail under loads experienced during the assembly process. However, like the liner mold, LIAD, and DIAD, it is recommended that final products of the diffuser tube be manufactured using steel. Shipping and handling of the aluminum tube was not considered as part of this work. It is not inconceivable that the tube may get damaged between the initial fabrication stage and the assembly stage; steel is more robust than aluminum and will resist damage effectively.

Large-scale manufacturing of the diffuser tube would lower material costs as large-batch raw material orders are often discounted compared to small-batch orders. It is also unlikely that each tube would be custom-fabricated in a machine shop. Custom machining, used for prototype fabrication, is expensive and time consuming. Large-scale manufacturing of the tube would require the development of an efficient, reusable mold.

CHAPTER 4

EXPERIMENTAL METHODOLOGY

Acoustic performance of in-line hydraulic suppressors can be quantitatively measured by the device transmission loss. The transmission loss of a given device is the ratio of upstream acoustic energy to downstream acoustic energy. More specifically, the transmission loss is defined as

$$TL = 10 \log_{10} \left| \frac{W_i}{W_t} \right|, \quad (4.1)$$

where W_i is incident acoustic energy and W_t is transmitted acoustic energy.

Although the device insertion loss can also be used to quantify device performance, device insertion loss is a property of the system as a whole rather than the device itself; therefore, an insertion loss measurement cannot be used to make conclusions about the device and inform other usages [11]. Unless certain circuit characteristics are known, the device insertion loss will not provide a useful measure of acoustic performance. The following sections of Chapter 4 focus on the experimental setup used to calculate the transmission loss. The chapter finishes with a discussion of sensor calibration and the concept of coherence.

4.1 Experimental Setup and Transmission Loss Calculation

A schematic of the experimental setup is shown in Figure 23. A Sauer Danfoss H1 bidirectional 9 piston pump provides flow to the system. The pump is driven by a Siemens 60 HP variable-speed AC motor operating at 1500 rpm. A needle valve

upstream of the test section provides broadband noise to the system. A downstream needle valve is used to restrict flow and achieve a predetermined system pressure. Static pressure sensors are placed on either side of the test component to measure the pressure drop across the device.

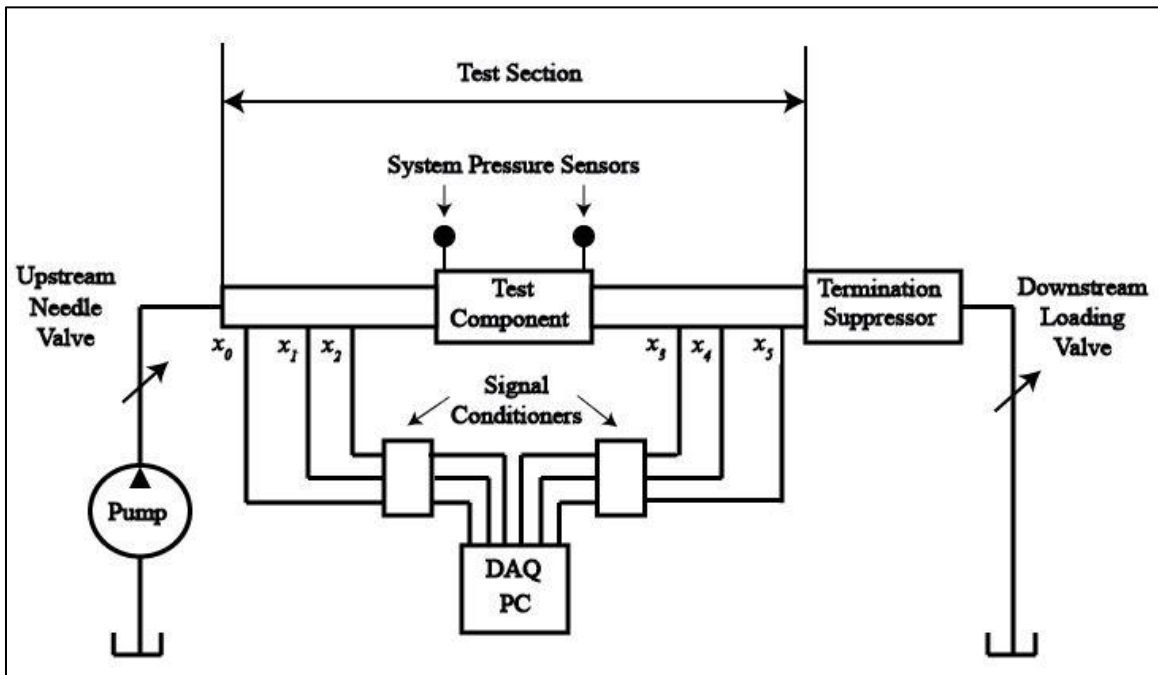


Figure 23: The hydraulic circuit used for suppressor testing

Three piezoelectric dynamic pressure sensors, PCB model 101A06, are placed at unequal intervals both upstream and downstream of the test component to collect transmission loss data. Unequal spacing of three sensors avoids half-wavelength indeterminacy issues which may arise when using only two sensors. When using two sensors, indeterminacy occurs at frequencies corresponding to an integer multiple of half wavelengths between the sensors [11]. To avoid half-wavelength indeterminacy,

transducers are placed at unequal intervals according to ISO-15086-2 [12]. Figure 24 illustrates relative distances between transducers in the test circuit.

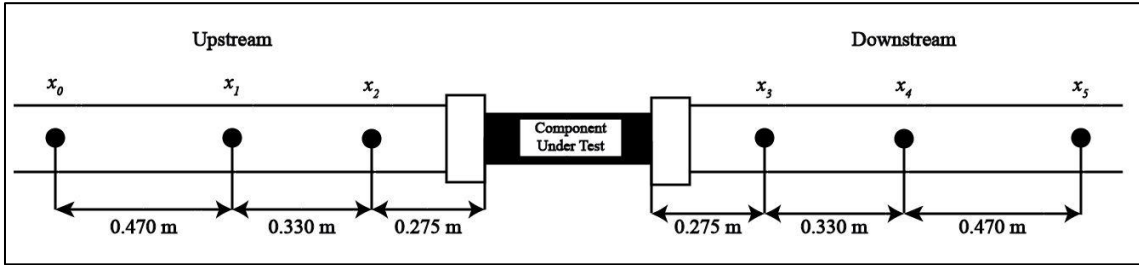


Figure 24: Dynamic pressure sensor spacing in experimental test section

The data acquisition (DAQ) system used in the experimental setup is an 8-channel, computer integrated acquisition board manufactured by National Instruments. Data is taken at 10800 samples per second with 5120 samples per data set. A single test run is the vector average of 30 data sets. Data was taken using National Instrument's LabVIEW 2014 software.

A transfer function, H_{ij} , relates measured data between sensor i and sensor j . Seven transfer functions are constructed to measure device transmission loss: two upstream functions, H_{01} and H_{21} , two downstream functions, H_{34} and H_{54} , and three across-component functions, H_{31} , H_{41} , and H_{51} .

The acoustic pressure in the upstream and downstream sections of the hydraulic circuit can be expressed with waves propagating in the positive and negative x-direction such that

$$P_{upstream} = (Ae^{-\gamma x} + Be^{\gamma x})e^{j\omega t}, \quad (4.2)$$

and

$$P_{\text{downstream}} = (Ee^{-\gamma x} + Fe^{\gamma x})e^{j\omega t}, \quad (4.3)$$

where A , B , E , and F are complex pressure wave amplitudes shown in Figure 25, and γ is the complex wavenumber.

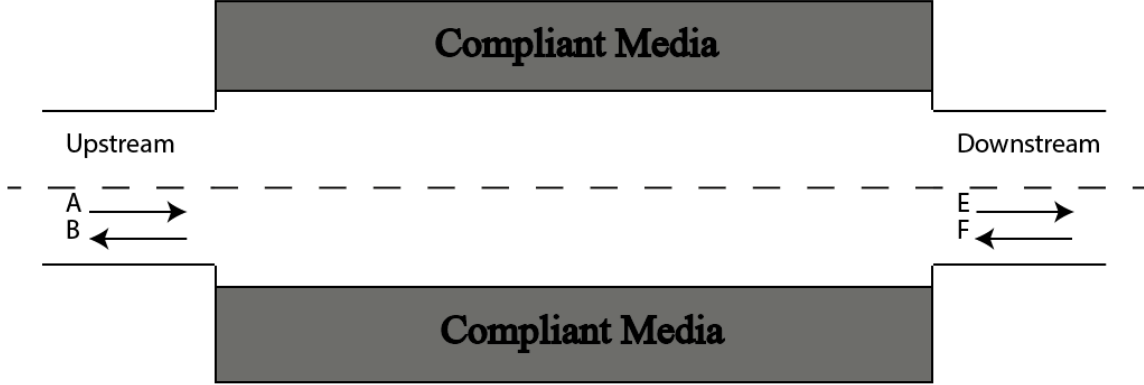


Figure 25: Upstream and downstream pressure amplitudes

Measured pressures at each sensor are placed in over-determined matrices, such that

$$M = \begin{bmatrix} e^{-\gamma x_0} & e^{\gamma x_0} \\ e^{-\gamma x_1} & e^{\gamma x_1} \\ e^{-\gamma x_2} & e^{\gamma x_2} \end{bmatrix}, \quad (4.4)$$

and

$$N = \begin{bmatrix} e^{-\gamma x_3} & e^{\gamma x_3} \\ e^{-\gamma x_4} & e^{\gamma x_4} \\ e^{-\gamma x_5} & e^{\gamma x_5} \end{bmatrix}. \quad (4.5)$$

Relative wave amplitudes are determined by solving the Moore-Penrose pseudoinverses

$$X = Mb, \quad (4.6)$$

and

$$Y = Nc. \quad (4.7)$$

In the preceding equations, the vectors X , Y , b , and c take the form of

$$X = \begin{pmatrix} A/p_1 \\ B/p_1 \end{pmatrix}, \quad (4.8)$$

$$Y = \begin{pmatrix} E/p_1 \\ F/p_1 \end{pmatrix}, \quad (4.9)$$

$$b = \begin{pmatrix} H_{01} \\ 1 \\ H_{21} \end{pmatrix}, \quad (4.10)$$

and

$$c = \begin{pmatrix} H_{31} \\ H_{41} \\ H_{51} \end{pmatrix}. \quad (4.11)$$

Equation (4.6) and Equation (4.7) allow for the computation of the complex wave amplitudes with respect to the pressure at sensor x_1 . The upstream and downstream volume velocities,

$$Q_{upstream} = \frac{(Ae^{-\gamma x} - Be^{\gamma x})}{Z_0} e^{j\omega t}, \quad (4.12)$$

and

$$Q_{downstream} = \frac{(Ee^{-\gamma x} - Fe^{\gamma x})}{Z_0} e^{j\omega t}, \quad (4.13)$$

are used in conjunction with the relative wave amplitudes to find the device transmission

loss. In the preceding equations, Z_0 is the specific impedance of the hydraulic fluid. A transfer matrix relates the pressure and volume velocity wave fields,

$$\begin{pmatrix} P_{upstream} \\ Q_{upstream} \end{pmatrix} = \begin{bmatrix} t_{11} & t_{12} \\ t_{21} & t_{22} \end{bmatrix} \begin{pmatrix} P_{downstream} \\ Q_{downstream} \end{pmatrix}. \quad (4.14)$$

Once the elements of the transfer matrix are computed, the device transmission loss can be calculated using

$$TL = 20 \log_{10} \left| \frac{1}{2} \left(t_{11} + \frac{t_{12}}{Z_0} + Z_0 t_{21} + t_{22} \right) \right|. \quad (4.15)$$

Assuming an acoustically reciprocal system and geometric symmetry of the test component [13],

$$t_{11} = t_{22}, \quad (4.16)$$

and

$$t_{21} = \frac{1 + t_{11}^2}{t_{12}}. \quad (4.17)$$

Using Equations (4.14), (4.16), and (4.17), the transfer matrix, T , can be rewritten as

$$T = \begin{bmatrix} 1 & -Z_0 \frac{A^2 + 2AB + B^2 - F^2 - 2EF - E^2}{A^2 - B^2 - F^2 + E^2} \\ -\frac{A^2 - 2AB + B^2 - F^2 + 2EF - E^2}{Z_0(A^2 - B^2 - F^2 + E^2)} & 1 \end{bmatrix}. \quad (4.18)$$

Substituting the above transfer matrix elements into Equation (4.15), transmission loss is then

$$TL = 20 \log_{10} \left| \frac{A^2 - F^2}{AE - BF} \right|. \quad (4.19)$$

By assuming an anechoic termination downstream of the test component, the

transmission loss can be rewritten as the ratio between the incident pressure amplitude and the transmitted pressure amplitude,

$$TL = 20 \log_{10} \left| \frac{A}{E} \right|. \quad (4.20)$$

It can be shown that only plane wave propagation occurs in the experimental test section. The assumption of plane wave mode propagation is important because it means that the pressure amplitude of the wave field is not angularly dependent and transducers can be mounted at any angle in the rig. Propagating waves in a waveguide are present for frequencies less than

$$\omega_m = ck_{lm}, \quad (4.21)$$

where c is the phase speed of sound, and k_{lm} is the acoustic wavenumber of mode (l,m) defined by,

$$k_{lm} = \frac{j'_{lm}}{a}. \quad (4.22)$$

In the preceding equation, j'_{lm} are input values that result in the extrema of $J_m(z)$, the m th order Bessel function of argument z , and a is radius of the pipe ID [8]. The limiting frequency in Equation (4.21) is known as the cutoff angular frequency. Wave modes with frequencies greater than the cutoff angular frequency result in evanescent waves that exponentially attenuate with distance from an acoustic source. Frequencies examined for this work are below 4000 Hz; the cutoff angular frequency corresponding to the first non-plane wave mode ($l=0,m=1$) is 43,000 Hz. The frequency range of interest for this work is well under the lowest non-plane wave mode cutoff angular frequency and only plane wave modes ($l=0,m=0$) propagate through the hydraulic circuit.

4.2 Sensor Calibration

Intrinsic manufacturing differences between dynamic pressure sensors cause slight variations in sensor response. Variations in sensor response are accounted for by conducting regular calibration of the sensors. A sensor calibration block, shown by Figure 26, is used to calibrate the sensors according to ISO 15086-2 [12]. The block is connected to a side branch (not shown) and installed as the test component in the hydraulic circuit. Four transducers are mounted in holes on each side of the block (not shown), which constrains the transducers to the same axial position. Because the ID of the calibration block is smaller than the ID of the test section, Equation (4.22) can be used to show that plane wave mode propagation occurs in the block across the entire frequency spectrum of interest (0 to 4000 Hz). Plane wave mode propagation in the block guarantees that each sensor is exposed to an identical wave field. Transfer functions between the sensors are created using data taken with a LabVIEW VI. Ideally, the magnitude of the transfer functions should be equal to 1 with a phase equal to 0° , but the calibration inherently accounts for slight deviations from these values.



Figure 26: The calibration block without sensors

4.3 Coherence

The coherence between two transducers is a measure of the linear correlation between the signals received by the sensors. Coherence values range from 0 to 1, with 0 indicating a non-linear correlation and 1 indicating a linear correlation between signals. High coherence values indicate highly correlated signals. The coherence is calculated in post-processing by

$$C_{ij} = \frac{|G_{ij}|^2}{G_{ii}G_{jj}} \quad (4.23)$$

where G_{ij} is the cross spectral density between sensors i and j , and G_{ii} and G_{jj} are autospectral densities. If any of the seven analyzed transfer functions have a coherence value less than 0.95 at a given frequency, the recorded data at that frequency is not

considered valid by ISO-15086-3 and is removed [14]. The coherence threshold is the reason for data dropout in the transmission loss results presented in the following chapter.

CHAPTER 5

SUPPRESSOR TRANSMISSION LOSS MEASUREMENTS

5.1 Suppressor Configuration Comparison

Transmission loss tests were conducted on all four suppressor configurations to compare device acoustic performance in accordance with the method described in Chapter 4. Devices were tested at four system pressures: 500 psi, 1000 psi, 1500 psi, and 2000 psi. Multiple system pressures were tested because hydraulic systems do not typically operate at a single system pressure. The pressure range chosen for testing reflects the expected operating range of hydraulic applications implementing the suppressors.

Figure 27 shows the transmission loss results for the suppressors at 500 psi system pressure. The liner, tube, and Grid1 configuration shows good acoustic performance across the tested frequency range. The Grid1 configuration shows particularly good results at the mid-range frequencies between 1500 Hz and 2000 Hz. A distinct null in transmission loss occurs at about 2000 Hz. Nulls in the transmission loss of expansion chamber suppressors occur at frequencies corresponding to integer multiples of

$$f_0 = \frac{c}{2L}, \quad (5.1)$$

where c is the speed of sound in the suppressor, and L is the suppressor length [15]. As system pressure increases, the speed of sound, c , in the suppressor increases and the frequency at which the first null occurs also increases.

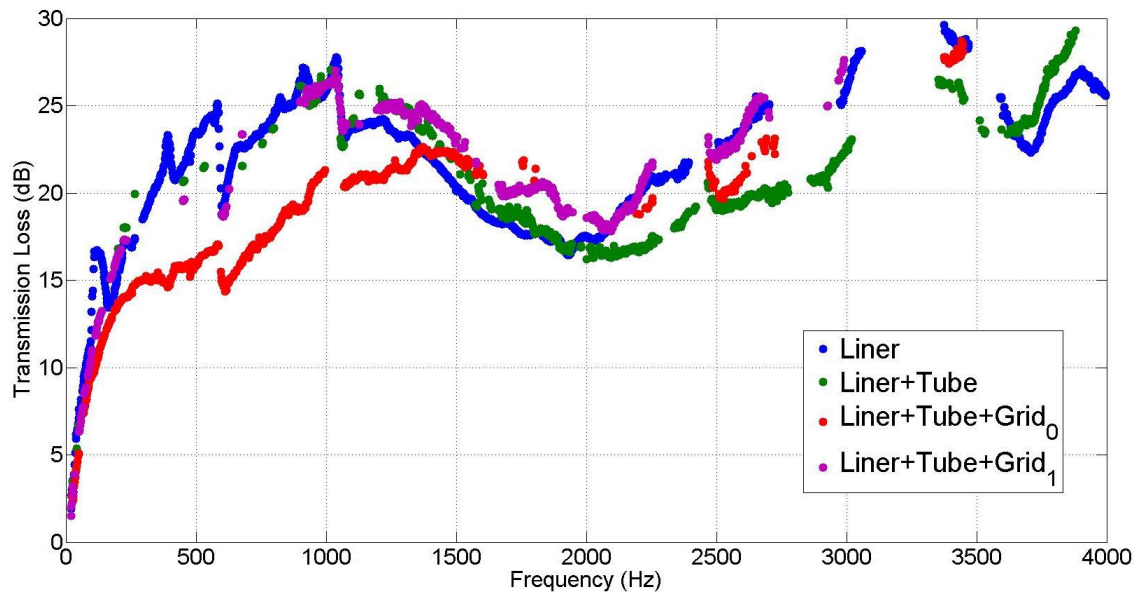


Figure 27: Comparison of transmission loss at a system pressure of 500 psi

Figure 28 shows transmission loss results for the suppressors at 1000 psi. The plain liner configuration, tube configuration, and Grid1 configuration show similar acoustic performance results, particularly at frequencies below 2000 Hz. The Grid0 configuration shows a slight decrease in performance at low frequencies compared to the other configurations. It is proposed that the resistivity of the Grid0 perforate sheet behaves too acoustically rigid at the low frequencies and therefore its transmission loss results are negatively impacted. The null in transmission loss results described by Equation (5.1) can not be seen in Figure 28 due to the high speed of sound inside the suppressor.

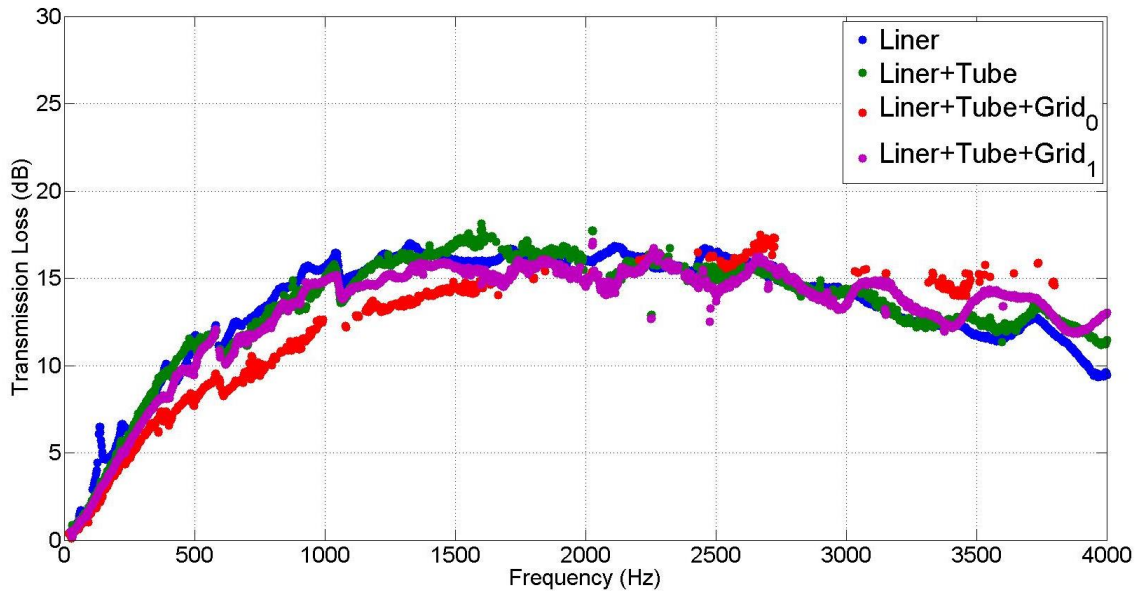


Figure 28: Comparison of transmission loss at a system pressure of 1000 psi

The transmission loss results for the suppressor configurations at 1500 psi are shown in Figure 29. The results presented by both Figure 28 and Figure 29 reveal that the acoustic performance of the suppressors declines with increased system pressure above 500 psi. The decline in acoustic performance is due to a decrease in microsphere void size under increased system pressure. Smaller voids reduce the total volume of compliant air in the liner which results in decreased acoustic performance. In Figure 29 it is important to note the data dropout of the tube configuration and the Grid0 configuration, particularly at high frequencies. The data dropout, which is attributed to coherence values (described in Chapter 4) below 0.95, are indicative of low linear correlation between acoustic signals upstream and downstream of the device. The data dropout is also evident in the previous figures, particularly for suppressors at 500 psi system pressure. At 500 psi system pressure, data dropout occurs when the upstream acoustic signal has been treated

to a magnitude below the measurement system noise floor. The high system noise relative to the attenuated downstream signal prevents the measurement technique (described in Chapter 4) from accurately determining the magnitude of the treated signal.

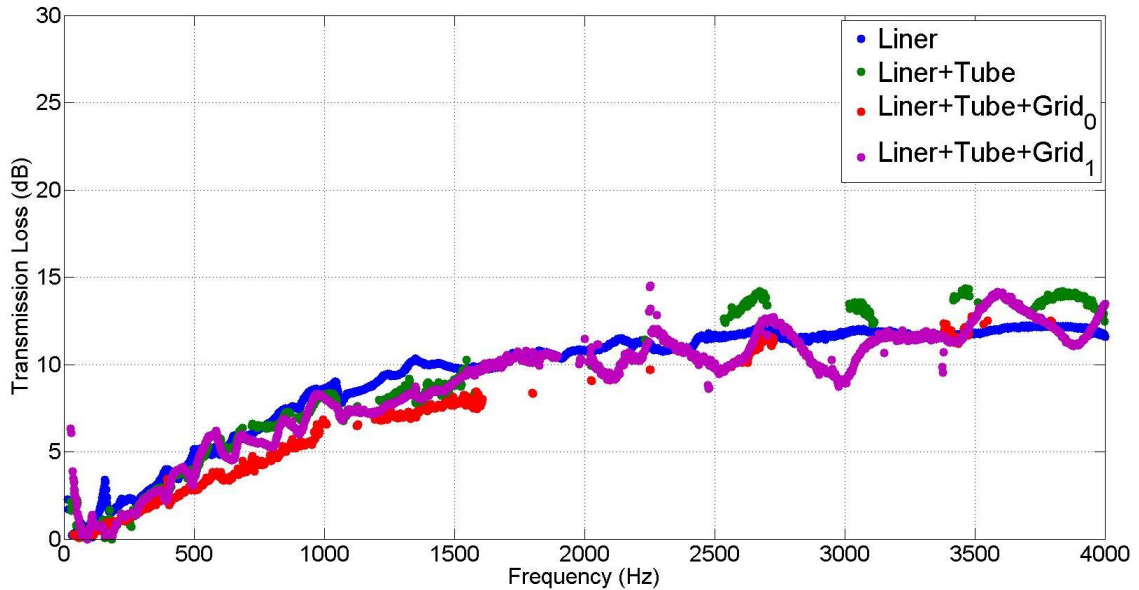


Figure 29: Comparison of transmission loss at a system pressure of 1500 psi

Acoustic performance results for the suppressor configurations at 2000 psi system pressure are shown in Figure 30. The performance of the suppressors has declined compared to their performance at the lower system pressures. A noticeable “ripple” in the Grid1 transmission loss results occurs at frequencies greater than 2000 Hz. The reason for this performance ripple is unknown as of the writing of this thesis.

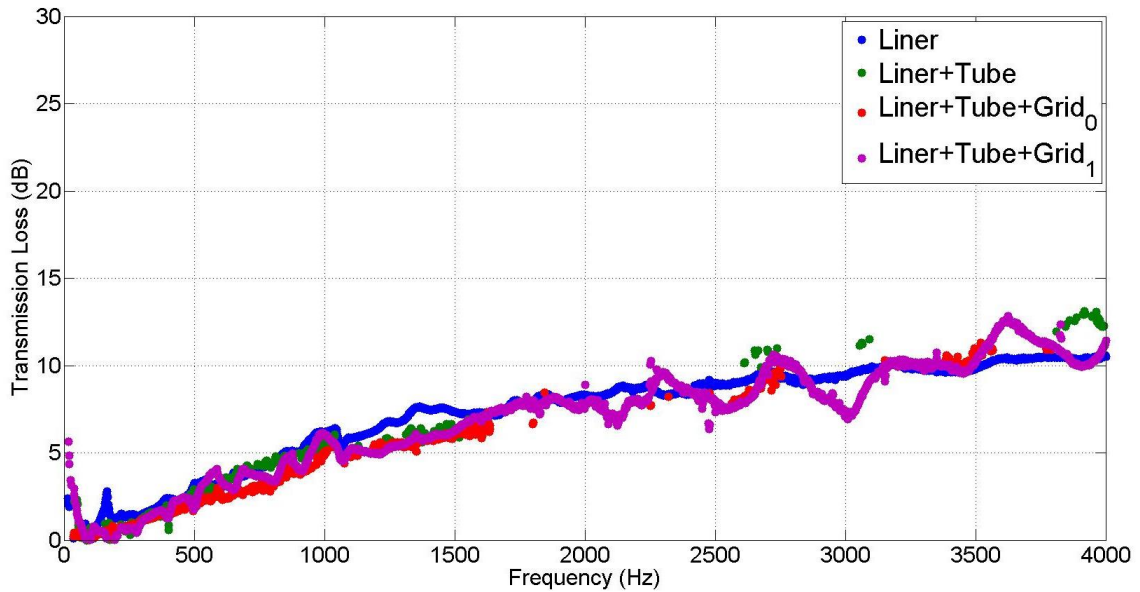


Figure 30: Comparison of transmission loss at a system pressure of 2000 psi

The suppressor configuration showing the highest transmission loss results for most of the tested frequencies and system pressures is the suppressor utilizing the liner, tube, and Grid1 arrangement. The suppressor shows superior results due to a combination of compliance from the liner and damping from the Grid1 perforate sheet. The resistivity of the Grid0 sheet (see Chapter 3) may have been too high to translate into any benefit in acoustic performance. The high resistivity of Grid0 causes the suppressor to behave acoustically rigid and dissipate little energy. The optimal resistivity of perforate sheets in terms of their acoustic performance in a liner-style suppressor is not currently known; future research on the subject is recommended for the successful commercialization and development of the liner-style suppressor.

5.2 Suppressor Repeatability Results

The Grid0 configuration data at 500 psi system pressure appears to be an outlier compared to the rest of the measured data. It was hypothesized that a change in oil temperature may have led to inaccurate results. Oil temperature in a test rig being run continuously rises with time; a change in oil temperature impacts the viscosity of the oil, which in turn affects the speed of sound in the oil and the transmission loss of the suppressor. Transmission loss data was collected with the rig running over a 20 minute period. Tests were taken at five equal intervals, five minutes apart.

Figure 31 shows the results of the repeatability test. There is a slight increase in performance between the zero minute test and the five minute test. The performance increase occurs for frequencies between 1000 Hz and about 2500 Hz. The temperature at the zero minute test was 32.00°F and the temperature at the five minute test was 32.12°F. After the first five minutes, rig temperatures and transmission loss results begin to stabilize. The final temperature of the rig was measured to be 32.14°F. The initial temperature and performance increase after the first five minutes is minimal and can be ignored in terms of the repeatability of the device results. The stability of the temperature and transmission loss results proves that the test results for the Grid0 configuration at 500 psi are real and repeatable. It is assumed that the repeatability is similar across all devices and system pressures.

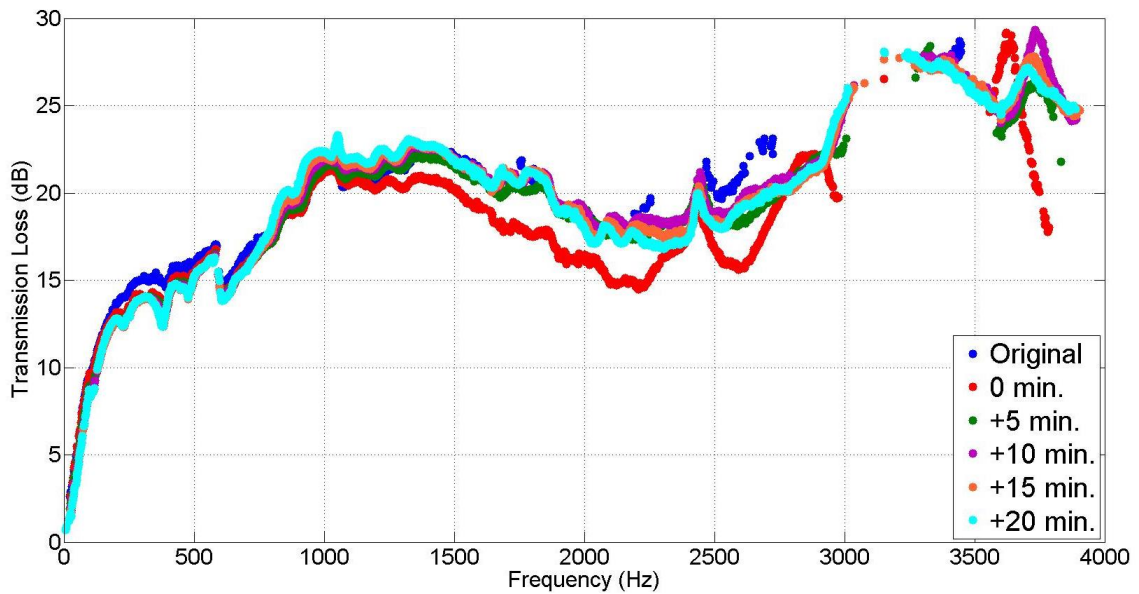


Figure 31: Repeatability test for the Grid0 configuration at 500 psi system pressure

5.3 Comparison Between Bladder-Style and Liner-Style Suppressors

Gruber et al. show that liner-style suppressors generally perform worse than equivalently sized bladder-style suppressors for system pressures less than or equal to 1000 psi [16]. Figure 32 shows that a bladder-style suppressor is capable of achieving a maximum transmission loss of over 25 dB at around 500 Hz and 1000 psi system pressure [16]. A liner-style suppressor at the same frequency and system pressure shows a 10 dB relative decrease in performance. The bladder-style suppressors in Figure 32 were charged to various pressures (ranging from 1.03 MPa to 6.21 MPa) as part of the work conducted by Gruber et al. All charge pressures shown in the figure, even those that are not optimal, out-perform the liner-style suppressor. The liner-style suppressor in Figure 32 is comprised of a plain liner and no diffusor. A comparison between liner-style

and bladder-style suppressors at system pressures greater than 1000 psi has not been documented to date. However, it is expected that bladder-style suppressors will acoustically outperform their liner-style counterparts at pressures greater than 1000 psi.

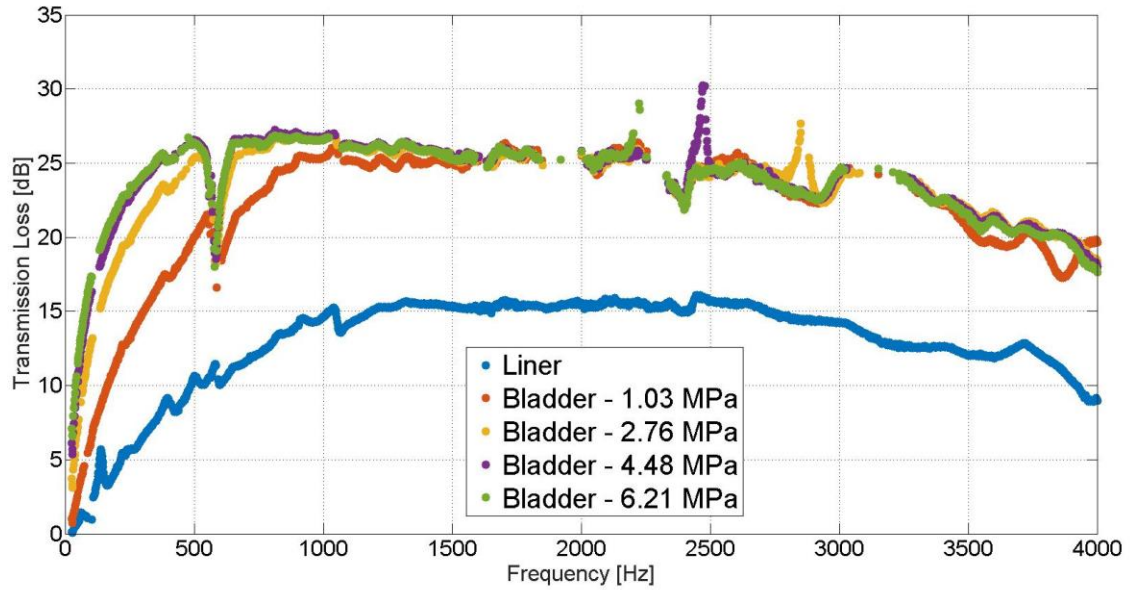


Figure 32: Comparison between bladder-style and liner-style suppressors [16]

CHAPTER 6

CONCLUSIONS

A simple and inexpensive fabrication and assembly method of a second generation liner-style suppressor has been developed. Four configurations were constructed for the purpose of this work: two configurations with a liner, diffuser tube, and perforate sheet, one configuration with a liner and diffuser tube, and one configuration with a plain liner. Prototypical assembly devices were made to assist with the insertion of the liner and diffuser into metal shells supplied by Wilkes & McLean.

Diffusers were constructed as part of the work for the purpose of improving suppressor acoustic performance, limiting suppressor self-noise, and reducing the possibility for microsphere shedding into the hydraulic circuit. An FEA was conducted on the diffuser tube body in order to avoid mechanical failure under loads experienced during the assembly process. The acoustic impedance and resistivity of two different photochemically etched, microperforate sheets was modeled in order to better understand their impact on the overall acoustic performance of the suppressors.

The acoustic performance of each configuration was tested at system pressures reflective of heavy machinery typical operating pressures. The configuration implementing the liner, diffuser tube, and Grid1 perforate sheet showed consistently high transmission loss results as compared to the other three tested configurations. The compliance and damping characteristics of the liner and Grid1 perforate sheet, respectively, resulted in good acoustic performance. Additionally, as an added bonus, the diffuser limits suppressor self-noise and reduces mechanical erosion of the liner.

6.1 Future Work

Further development of this work should be focused on three areas: final product manufacturing, accurate measurement of liner self-noise and mechanical erosion, and perforate sheet impact on overall suppressor acoustic performance. Future generations of the liner-style suppressor should consider improving manufacturing methods for the bulk production of liners and diffusors. The effectiveness of proposed large-scale liner and diffusor molds would need to be examined in terms of their precision, robustness, and production output. The individually cast liners and custom-machined diffusors created for the purpose of this thesis require far too much time and labor to be considered a commercially viable option for large-scale production.

The amount of self-noise produced by suppressor configurations was not investigated as part of this work. Although it is known that the diffusor reduces turbulence-induced self-noise, the exact amount of reduction is not currently known. Flow meters placed upstream and downstream of the suppressor can measure changes in flow rate through a given suppressor. It is assumed that the change in flow rate is proportional to downstream liner self-noise but this will need to be validated through rigorous testing. Long term observation of the liner in a hydraulic circuit will reveal important information about microsphere shedding. A filter small enough to trap microspheres averaging 80 microns in diameter [17] would need to be purchased and installed downstream of the suppressor. The filter would allow for a way to measure the effectiveness of a given diffusor at preventing mechanical erosion of the liner.

Perforate sheet impedance modeling needs to be improved in order to accurately predict sheet impact on transmission loss. Work has been done on the predicted impact of sheet impedance on bladder-style transmission loss [18]. However, it is unclear whether this work translates to the performance of liner-style suppressors. Multiple sheets should be tested in various liner-style configurations in order to validate existing performance prediction models. The work presented in this thesis examined only two types of perforate sheets that were readily available and free of charge. Future work should examine the performance results of several perforate sheets without regard to cost.

APPENDIX A

ENGINEERING DRAWINGS

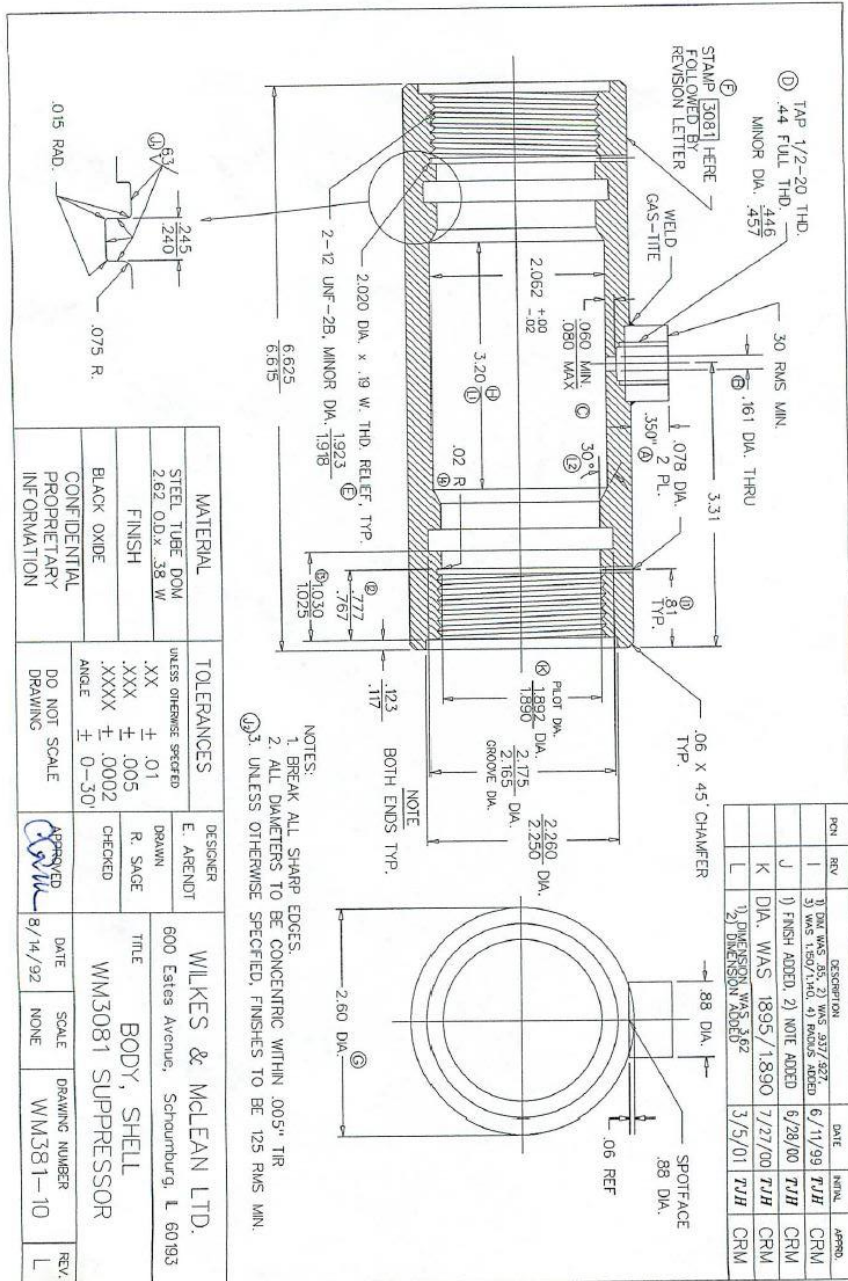


Figure 33: WM3081 suppressor outer shell drawing [19]

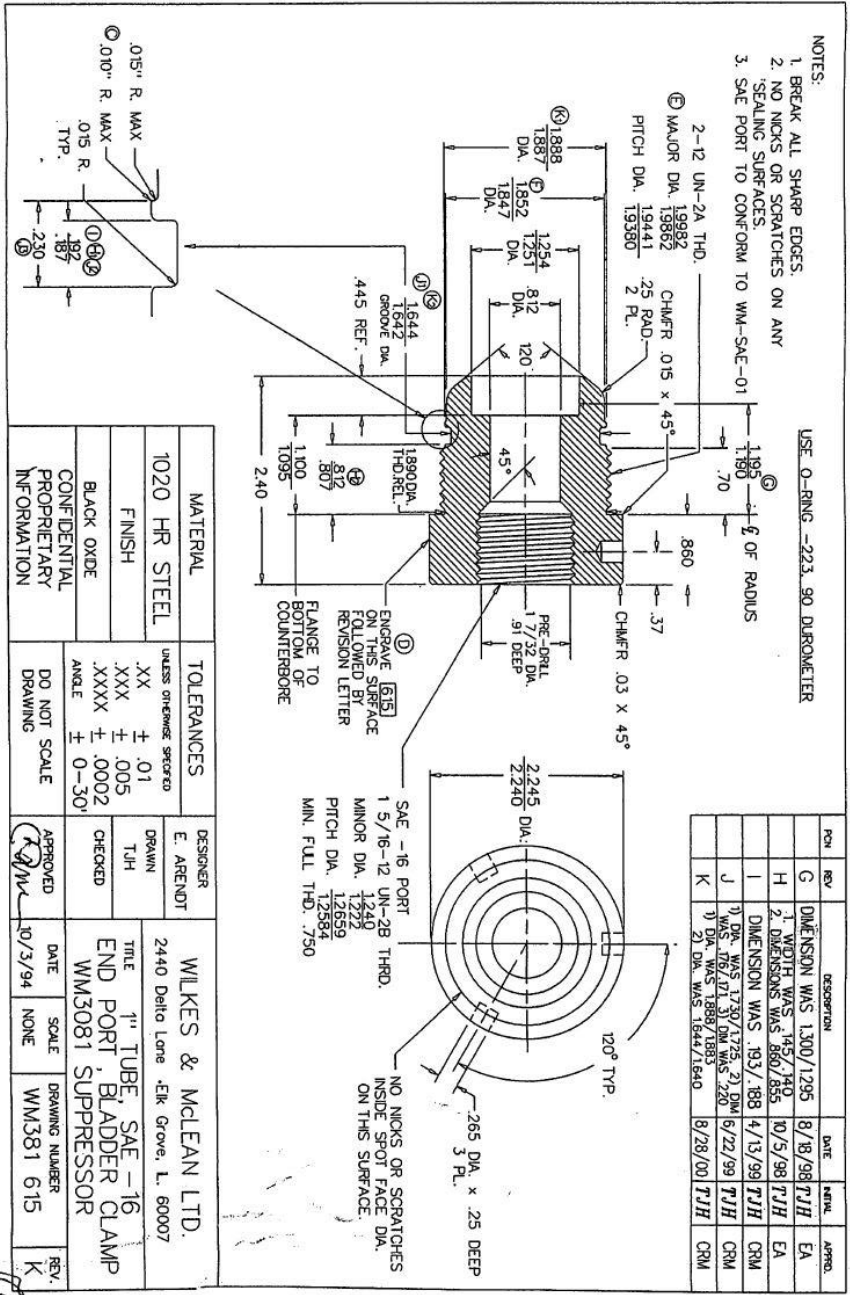


Figure 34: WM3081 suppressor end cap drawing [19]

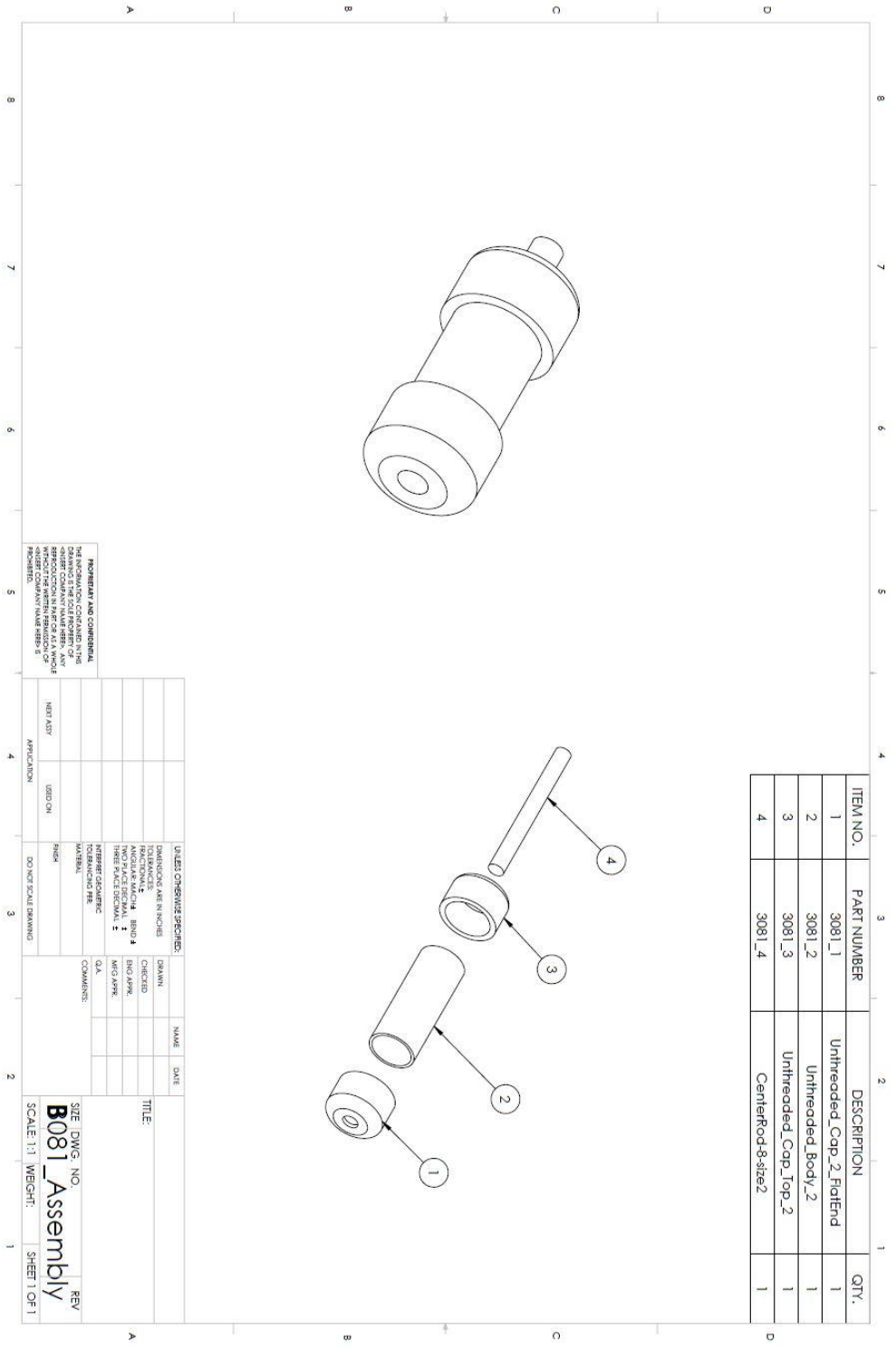


Figure 35: WM3081 liner mold assembly

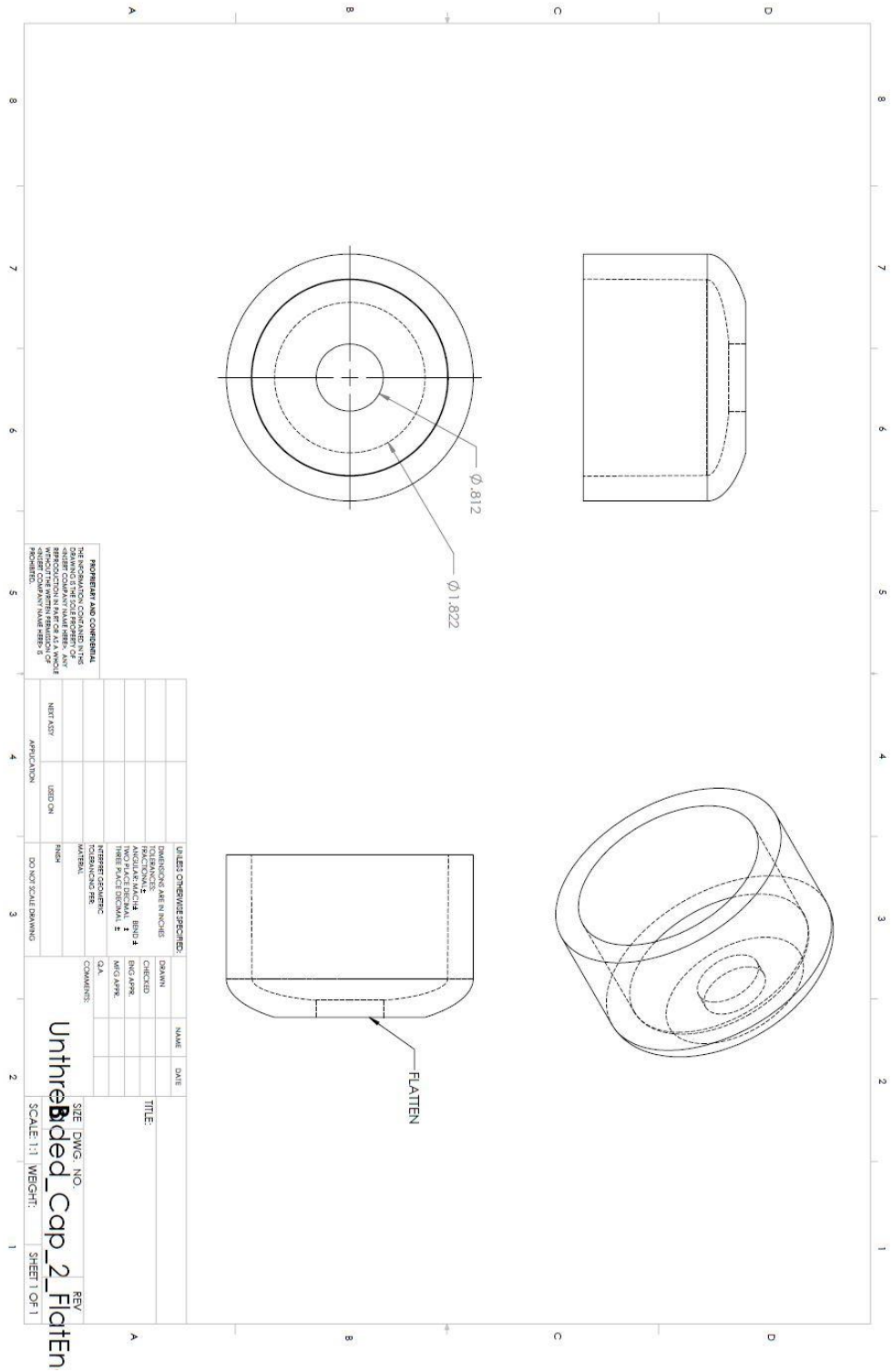


Figure 36: Liner mold bottom end cap drawing

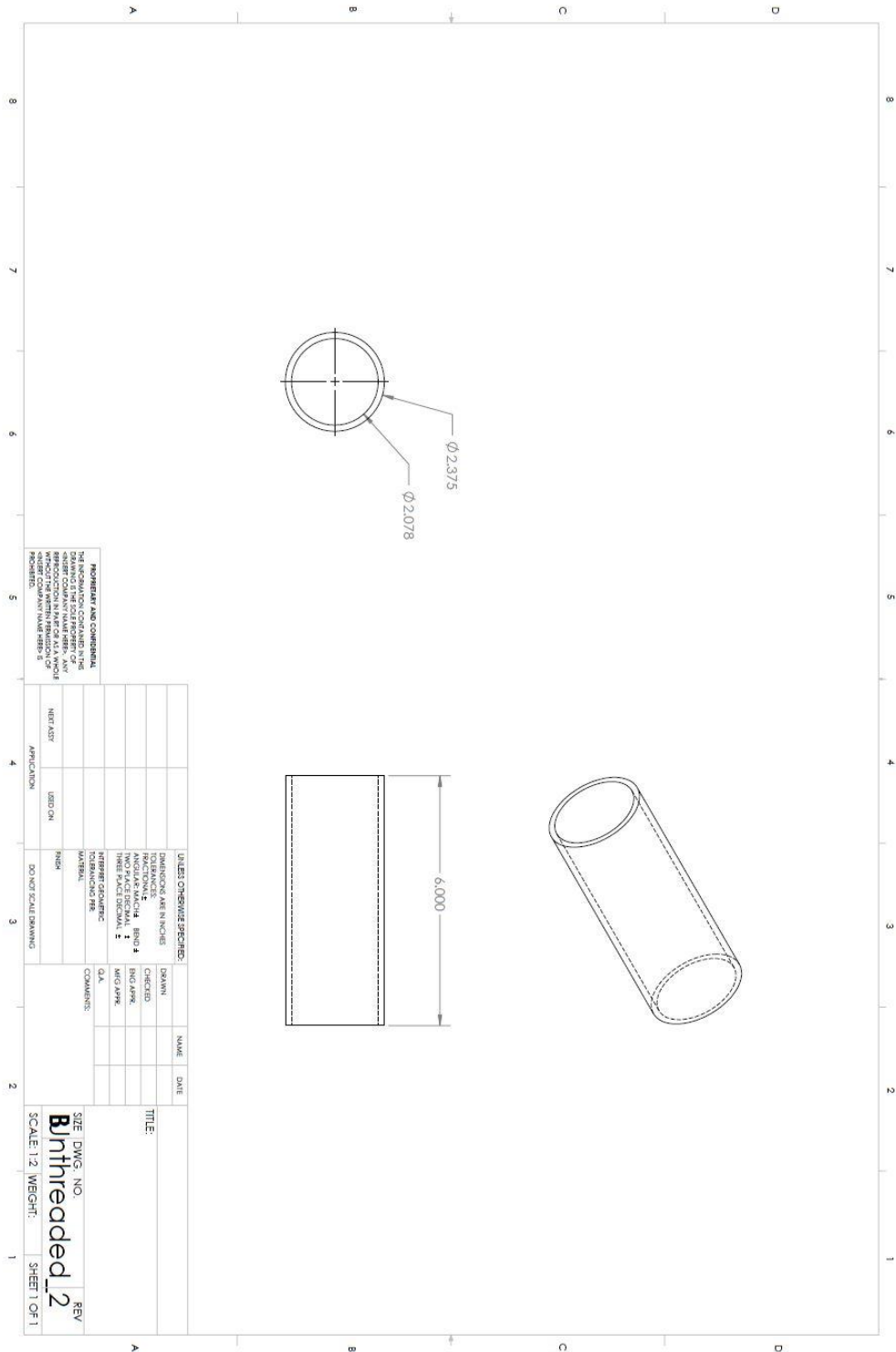


Figure 37: Liner mold body drawing

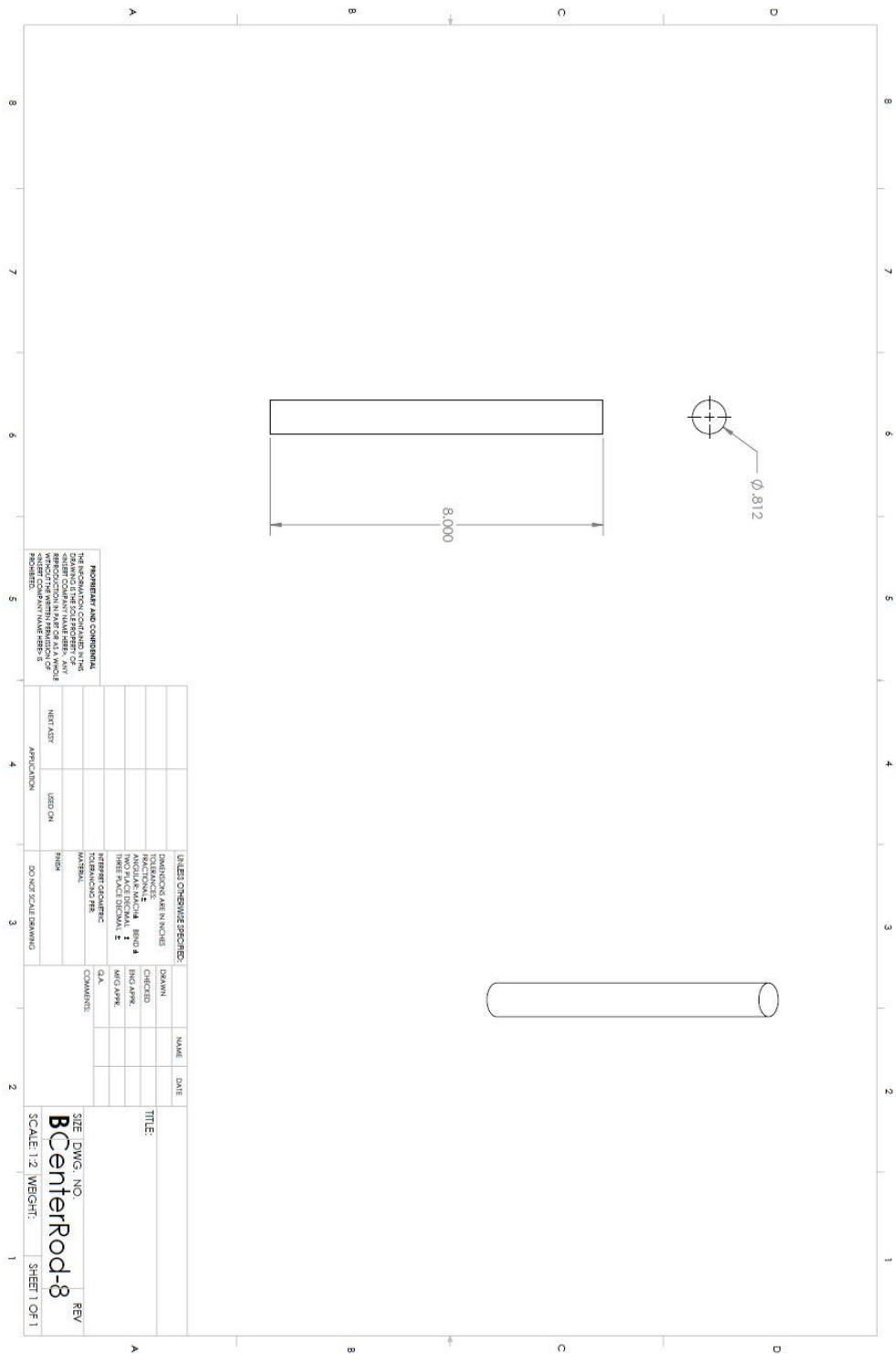


Figure 39: Liner mold center rod drawing

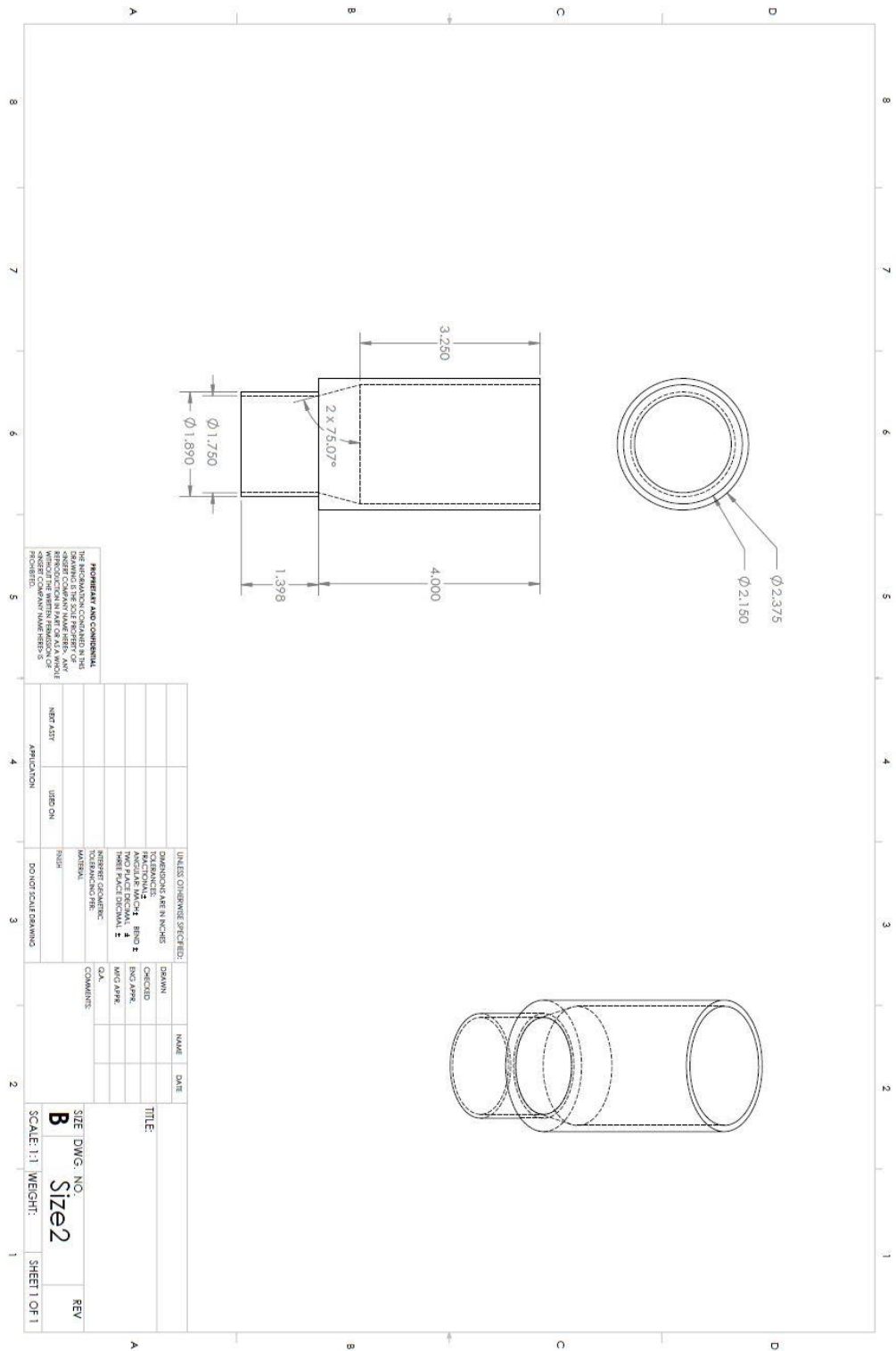
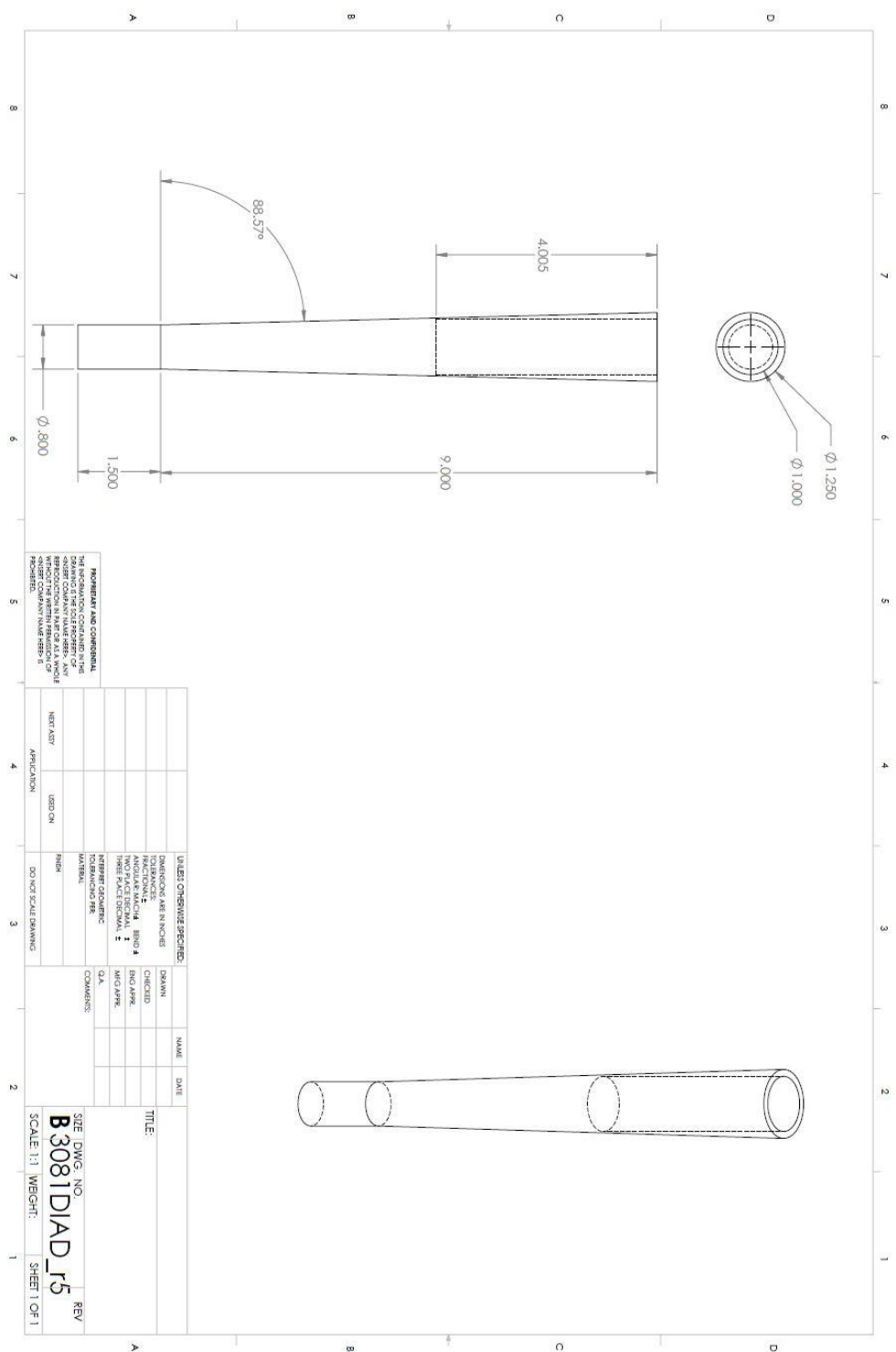


Figure 40: LIAD drawing



NONREPEATABLE COMPONENTS
 THE DIMENSIONS OF THIS DRAWING TO THE FURTHER RIGHT OF THIS LINE ARE NOT TO BE USED TO REPRODUCE THIS DRAWING WITHOUT THE WRITTEN PERMISSION OF THE ORIGINAL DRAWING ENGINEER. (SEE DRAWING NOTES FOR MORE INFORMATION.)

DATE	NAME	DESCRIPTION

SHEET NO. B3081DIAD_r5
SCALE: 1:1
WEIGHT:
SHEET 1 OF 1

Figure 41: DIAD drawing

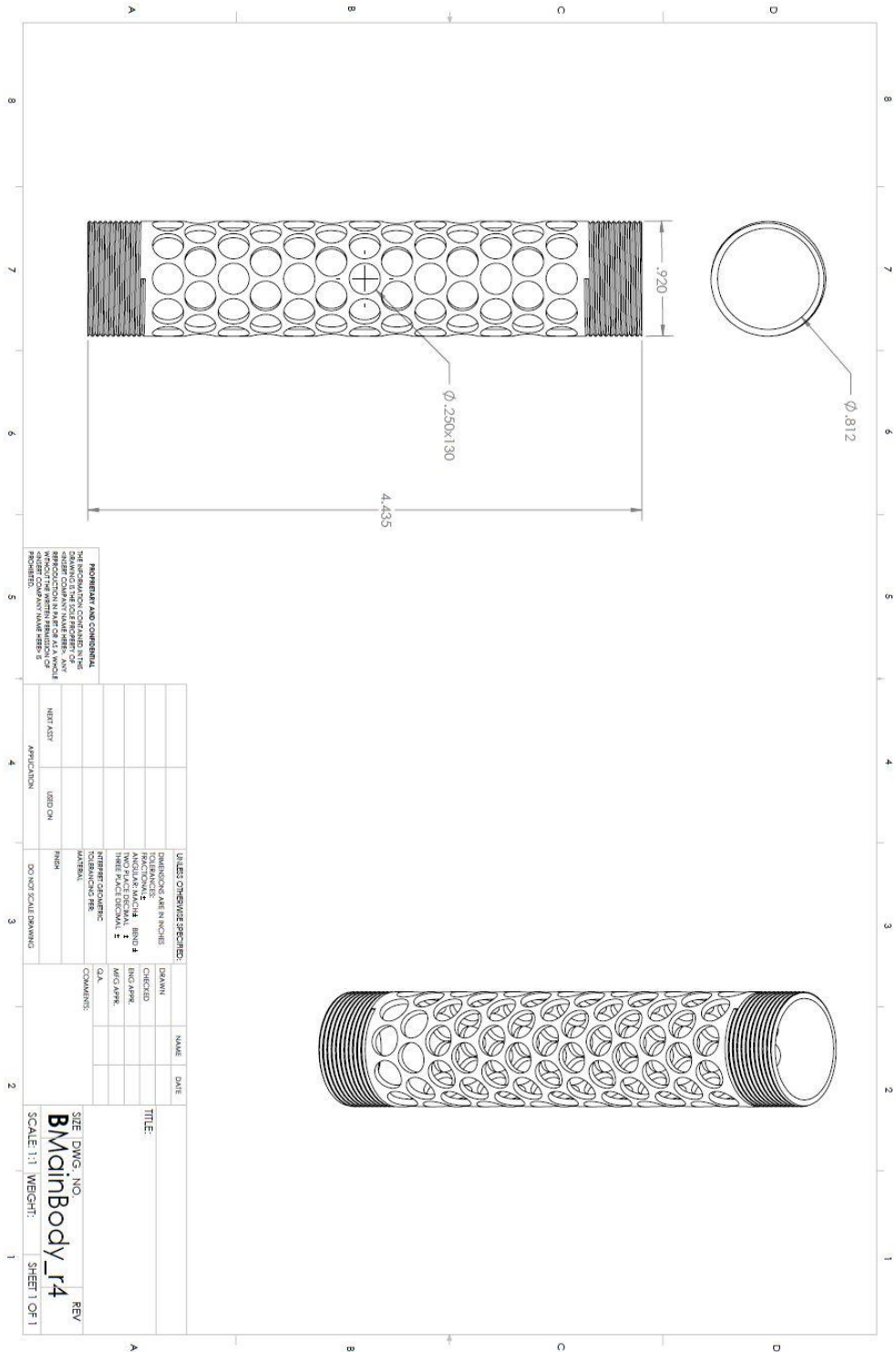


Figure 42: Diffusor tube drawing

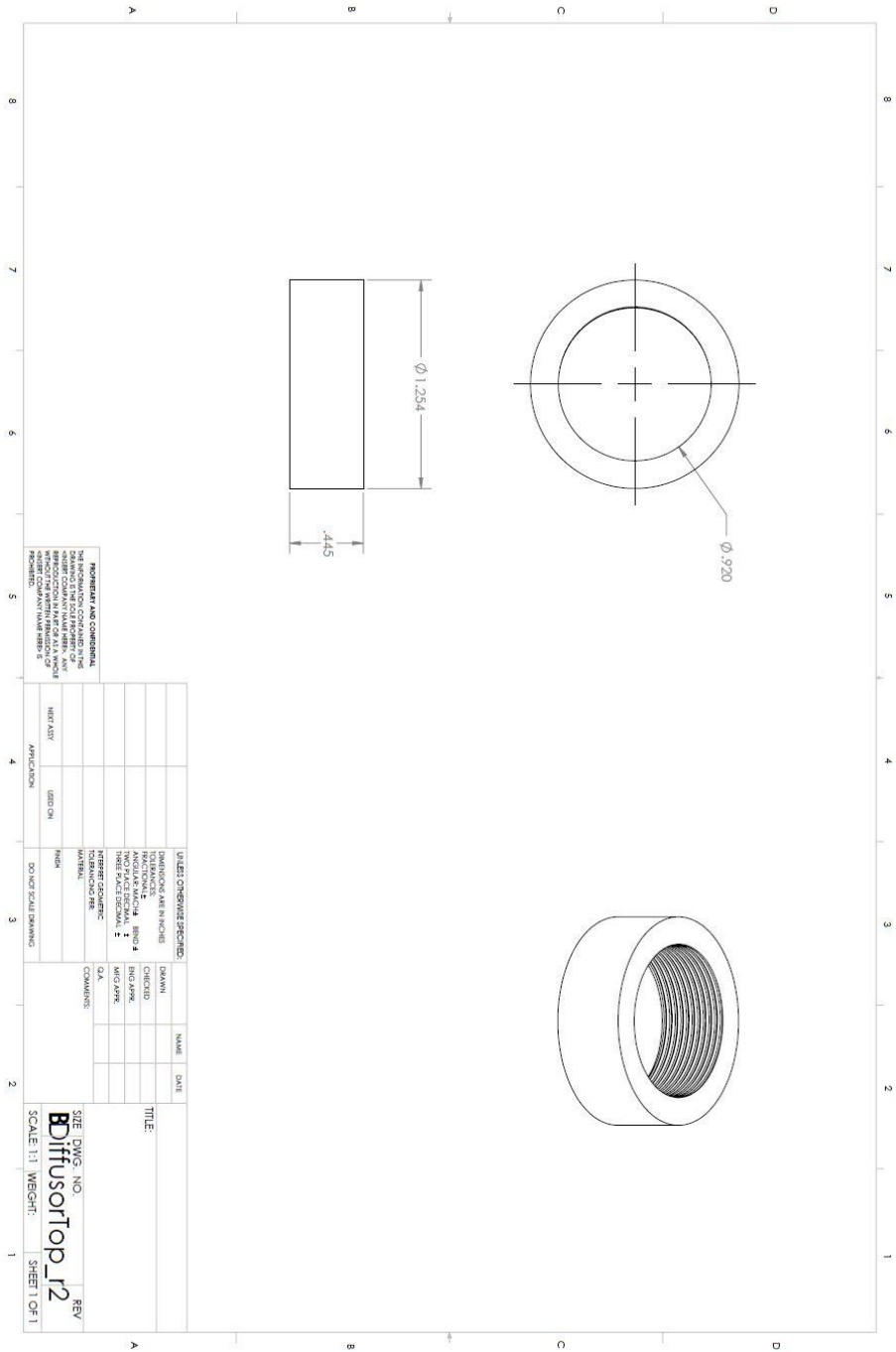


Figure 43: Diffusor end cap drawing

APPENDIX B

MATLAB CODE

Radial Stress Iteration

```
clear all
clc

load('wrkspc', 'composite')

E = real(composite.youngs);
v = real(composite.poisson);
C1 = 2.0*10^-1;
C2 = -4.5*10^-5;
r = 2.3*10^-2;

tolerance=0.01;
delta=9999;

i=1;
k=1;
Sigma(i)=0;

while delta > tolerance
    Sigma(i+1)=((E(k)./(1-(v(k).^2))).*((C1.*(1+v(k)))-(C2.*(1-
v(k))./(r.^2))));
    k=round(Sigma(i+1)/(1.37e3));%1.37e3 Pa is the pressure interval
between indices in E and v
    delta=(Sigma(i+1)-Sigma(i))./(Sigma(i+1));
    i=i+1;
end

disp(Sigma)%units are Pa
```

Diffusor Impedance Calculations

```
%Diffusor Tube Impedance Calculations
%Last Updated: 11/17/2015

clear all
clc

%Tube Impedance Calculations

f = 0:1:4000; %frequency, hz

N = 130; %number of holes
r = (6.35*10^-3)/2; %radius of a hole, m
A = pi*r^2; %area of a hole, m^2
S = 2*pi*(0.0234/2)*(0.0897); %total area of tube (no holes), m^2
P = (100*N*A)/S; %percent open area

rho = 861; %density of oil, kg/m^3
c = 1400; %speed of sound in oil, m/s
k = (2*pi*f)/c; %wavenumber, m^-1
l = 2.74*10^-3; %effective length of a hole, m

w = 2.74*10^-3; %length of a hole, m
D = 2*pi*r; %perimeter of a hole, m
mu = 3.96*10^-2; %fluid viscosity, kg/(ms)
t = sqrt(mu./(rho*pi*f)); %boundary layer thickness
h = w/2; %half plate thickness

R = ((rho*c)/A)*(((k.*t*D*w)/(2*A)) +
(0.288*k.*t*log10((4*A)/(pi*h^2)))); %Acoustic resistance
Z = (100/(P*S))*((R*A) + 1i*(rho*c*tan(k*l))); %Tube Impedance

%Characteristic Fluid Impedance

A_pipe = pi*(0.019/2)^2;
Z_pipe = (rho*c)/A_pipe;
Z_p = length(f);

for i = 1:length(f)
    Z_p(i)=Z_pipe;
end

%Plotting Functions

figure(1)
loglog(f,Z_p,f,abs(Z))
xlabel('Frequency [Hz]')
ylabel('Impedance [rayl]')

figure(2)
subplot(2,1,1)
```



```
plot(f, real(Z))
xlabel('Frequency [Hz]')
ylabel('Acoustic Resistance, R_A')
subplot(2,1,2)
plot(f, imag(Z))
xlabel('Frequency [Hz]')
ylabel('Acoustic Reactance, X_A')
```

```

%Diffusor Tube+Grid0 Impedance Calculations
%Last Updated: 11/17/2015

clear all
clc

%Tube Impedance Calculations

f = 0:1:4000; %frequency, hz

N = 130; %number of holes in tube
r = (6.35*10^-3)/2; %radius of a hole, m
A = pi*r^2; %area of a hole, m^2
S = 2*pi*(0.0234/2)*(0.0897); %surface area of tube (no holes), m^2
P = (100*N*A)/S; %percent open area

rho = 861; %density of oil, kg/m^3
c = 1400; %speed of sound in oil, m/s
k = (2*pi*f)/c; %wavenumber, m^-1
l = 2.74*10^-3; %effective length of a hole, m

w = 2.74*10^-3; %length of a hole, m
D = 2*pi*r; %perimeter of a hole, m
mu = 3.96*10^-2; %fluid viscosity, kg/(ms)
t = sqrt(mu./(rho*pi*f)); %boundary layer thickness
h = w/2; %half plate thickness

R = ((rho*c)/A)*(((k.*t*D*w)/(2*A)) +
(0.288*k.*t*log10((4*A)/(pi*h^2)))); %Acoustic resistance
Z = (100/(P*S))*((R*A) + li*(rho*c*tan(k*l))); %Tube Impedance

%Grid_0 Impedance Calculations

f_g0 = 0:1:4000; %frequency, hz

N_g0 = 26; %number of holes in sample
r_g0 = (1.6*10^-4)/2; %radius of a hole, m
A_g0 = pi*r_g0^2; %area of a hole, m^2
S_0_g0 = 0.001211*0.001624; %area of sample perforate sheet w/o holes,
m^2
P_g0 = (100*N_g0*A_g0)/S_0_g0; %percent open area
S_g0 = 0.0889*0.0762; %area of total perforate sheet used, m^2

rho_g0 = 861; %density of oil, kg/m^3
c_g0 = 1400; %speed of sound in oil, m/s
k_g0 = (2*pi*f_g0)/c_g0; %wavenumber, m^-1
l_g0 = 0.00012; %effective length of a hole, m

w_g0 = 0.00012; %length of a hole, m
D_g0 = 2*pi*r_g0; %perimeter of a hole, m
mu_g0 = 3.96*10^-2; %fluid viscosity, kg/(ms)
t_g0 = sqrt(mu_g0./(rho_g0*pi*f_g0)); %boundary layer thickness
h_g0 = w_g0/2; %half plate thickness

```

```

R_g0 = ((rho_g0*c_g0)/A_g0)*(((k_g0.*t_g0*D_g0*w_g0)/(2*A_g0)) +
(0.288*k_g0.*t_g0*log10((4*A_g0)/(pi*h_g0^2)))); %Acoustic resistance
Z_g0 = (100/(P_g0*S_g0))*(R_g0*A_g0) +
1i*(rho_g0*c_g0*tan(k_g0*l_g0)); %Impedance

%Total Impedance

Z_tot = abs(Z)+abs(Z_g0);

%Plotting Functions

figure(1)
plot(f,abs(Z_tot))
xlabel('Frequency [Hz]')
ylabel('Impedance [rayl]')

figure(2)
subplot(2,1,1)
plot(f,real(Z_tot))
xlabel('Frequency [Hz]')
ylabel('Acoustic Resistance, R_A')
subplot(2,1,2)
plot(f,imag(Z_tot))
xlabel('Frequency [Hz]')
ylabel('Acoustic Reactance, X_A')

```

```

%Diffusor Tube+Grid1 Impedance Calculations
%Last Updated: 11/17/2015

clear all
clc

%Tube Impedance Calculations

f = 0:1:4000; %frequency, hz

N = 130; %number of holes
r = (6.35*10^-3)/2; %radius of a hole, m
A = pi*r^2; %area of a hole, m^2
S = 2*pi*(0.0234/2)*(0.0897); %total area of tube (no holes), m^2
P = (100*N*A)/S; %percent open area

rho = 861; %density of oil, kg/m^3
c = 1400; %speed of sound in oil, m/s
k = (2*pi*f)/c; %wavenumber, m^-1
l = 2.74*10^-3; %effective length of a hole, m

w = 2.74*10^-3; %length of a hole, m
D = 2*pi*r; %perimeter of a hole, m
mu = 3.96*10^-2; %fluid viscosity, kg/(ms)
t = sqrt(mu./(rho*pi*f)); %boundary layer thickness
h = w/2; %half plate thickness

R = ((rho*c)/A)*(((k.*t*D*w)/(2*A)) +
(0.288*k.*t*log10((4*A)/(pi*h^2)))); %Acoustic resistance
Z = (100/(P*S))*((R*A) + li*(rho*c*tan(k*l))); %Tube Impedance

%Grid_1 Impedance Calculations

f_g1 = 0:1:4000; %frequency, hz

r_g1 = ((0.02*25400)*10^-6)/2; %radius of a hole, m
A_g1 = pi*r_g1^2; %area of a hole, m^2
S_g1 = 0.0889*0.0762; %area of total perforate sheet, m^2
P_g1 = 22; %percent open area

rho_g1 = 861; %density of oil, kg/m^3
c_g1 = 1400; %speed of sound in oil, m/s
k_g1 = (2*pi*f_g1)/c_g1; %wavenumber, m^-1
l_g1 = 0.008*0.0254; %effective length of a hole, m

w_g1 = l_g1; %length of a hole, m
D_g1 = 2*pi*r_g1; %perimeter of a hole, m
mu_g1 = 3.96*10^-2; %fluid viscosity, kg/(ms)
t_g1 = sqrt(mu_g1./(rho_g1*pi*f_g1)); %boundary layer thickness
h_g1 = w_g1/2; %half plate thickness

```

```

R_g1 = ((rho_g1*c_g1)/A_g1)*(((k_g1.*t_g1*D_g1*w_g1)/(2*A_g1)) +
(0.288*k_g1.*t_g1*log10((4*A_g1)/(pi*h_g1^2)))); %Acoustic resistance
Z_g1 = (100/(P_g1*S_g1))*(R_g1*A_g1) +
1i*(rho_g1*c_g1*tan(k_g1*l_g1)); %Impedance

%Total Impedance

Z_tot = abs(Z)+abs(Z_g1);

%Plotting Functions


figure(1)
plot(f,abs(Z_tot))
xlabel('Frequency [Hz]')
ylabel('Impedance [rayl]')

figure(2)
subplot(2,1,1)
plot(f,real(Z_tot))
xlabel('Frequency [Hz]')
ylabel('Acoustic Resistance, R_A')
subplot(2,1,2)
plot(f,imag(Z_tot))
xlabel('Frequency [Hz]')
ylabel('Acoustic Reactance, X_A')

```

APPENDIX C

TUBE FEA ANALYSIS REPORT



A 3D CAD model of a vertical cylindrical tube with a complex, lattice-like perforated structure. The tube is shown in a perspective view against a light blue background. A small coordinate system icon is visible in the bottom-left corner of the image area.

Simulation of MainBody_r4


Date: Sunday, November 08, 2015
Designer: Ryan Salmon
Study name: Static 1
Analysis type: Static

Table of Contents

- Model Information.....2
- Study Properties3
- Units.....4
- Material Properties.....4
- Loads and Fixtures.....5
- Mesh information6
- Resultant Forces.....8
- Study Results.....9


□

Model Information



Model name: MainBody_r4
Current Configuration: Default

Solid Bodies			
Document Name and Reference	Treated As	Volumetric Properties	Document Path/Date Modified

<p>LPattern2</p> 	<p>Solid Body</p>	<p>Mass:0.0125566 kg Volume:4.65058e-006 m³ Density:2700 kg/m³ Weight:0.123054 N</p>	<p>C:\Research\SW Diffusor Drawings\3081\MainBody_r4.SLDPRT Oct 30 12:43:42 2015</p>
--	-------------------	--	--


Study Properties

Study name	Static 1
Analysis type	Static
Mesh type	Solid Mesh
Thermal Effect:	On
Thermal option	Include temperature loads
Zero strain temperature	298 Kelvin
Include fluid pressure effects from SOLIDWORKS Flow Simulation	Off
Solver type	FEPlus
Inplane Effect:	Off
Soft Spring:	Off
Inertial Relief:	Off
Incompatible bonding options	Automatic
Large displacement	Off
Compute free body forces	On
Friction	Off
Use Adaptive Method:	Off
Result folder	SOLIDWORKS document (C:\Research\SW Diffusor Drawings\3081)

Units

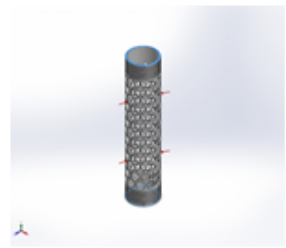
Unit system:	SI (MKS)
Length/Displacement	mm
Temperature	Kelvin
Angular velocity	Rad/sec
Pressure/Stress	N/m ²

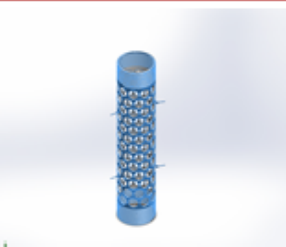
Material Properties

Model Reference	Properties	Components
	<p>Name: Aluminum Model type: Linear Elastic Isotropic Default failure criterion: Max von <u>Mises</u> Stress Yield strength: 2.41317e+008 N/m² Elastic modulus: 6.9e+010 N/m² Poisson's ratio: 0.33 Mass density: 2700 kg/m³</p>	<p><u>SolidBody</u> 1(LPatten2)(MainBody_r4)</p>
Curve Data: <u>N/A</u>		



Loads and Fixtures

Fixture name	Fixture Image	Fixture Details		
Fixed-1		Entities: 2 face(s) Type: Fixed Geometry		
Resultant Forces				
Components	X	Y	Z	Resultant
Reaction force(N)	-441.873	-1.64034	80.4979	449.149
Reaction Moment(N.m)	0	0	0	0

Load name	Load Image	Load Details
Pressure-1		Entities: 1 face(s) Type: Normal to selected face Value: 1.97e+007 Units: N/m^2 Phase Angle: 0 Units: deg

Mesh information

Mesh type	Solid Mesh
Mesh Used:	Curvature based mesh
Jacobian points	4 Points
Maximum element size	0.0854121 in
Minimum element size	0.0854121 in
Mesh Quality	High

Mesh information - Details

Total Nodes	28121
Total Elements	12564
Maximum Aspect Ratio	182.96
% of elements with Aspect Ratio < 3	60.1
% of elements with Aspect Ratio > 10	10.8
% of distorted elements(Jacobian)	0
Time to complete mesh(hh:mm:ss):	00:00:09
Computer name:	ME00824





Resultant Forces

Reaction forces

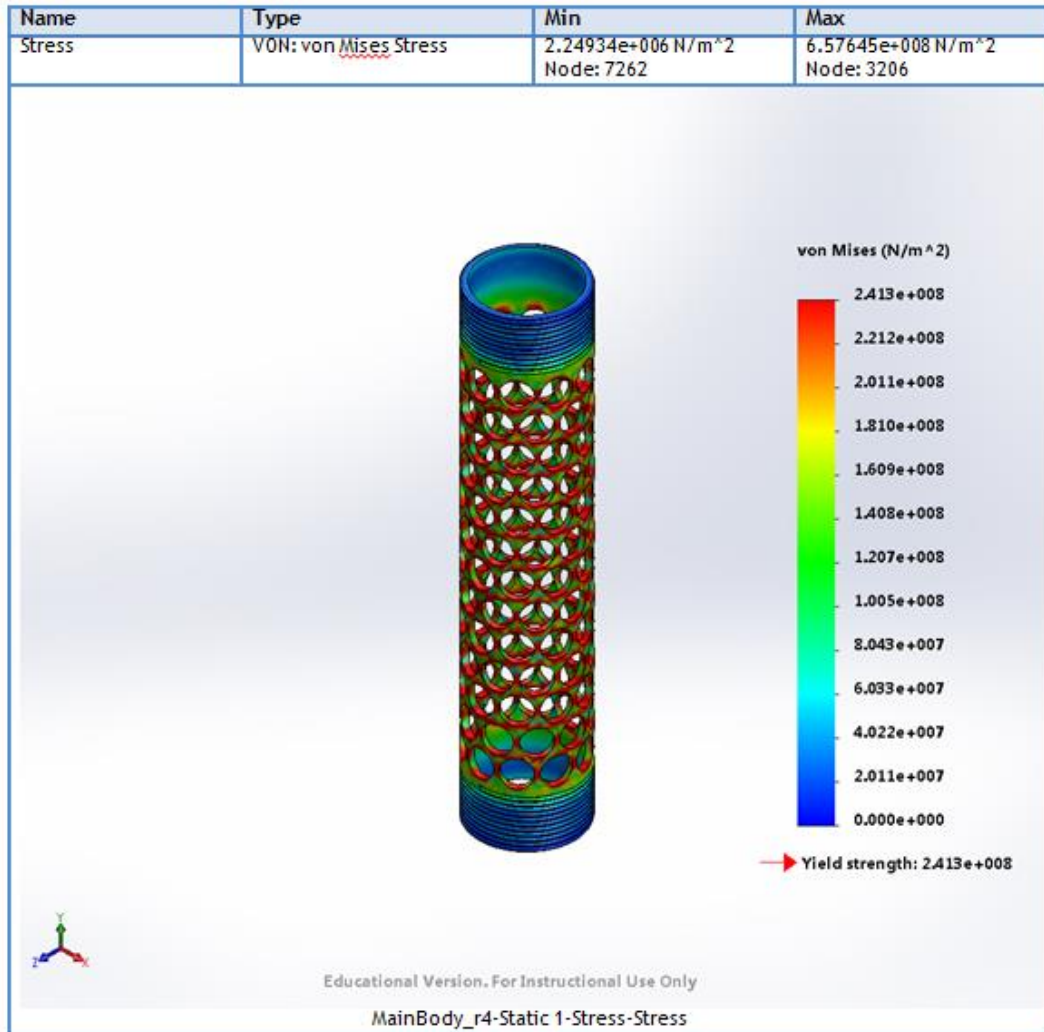
Selection set	Units	Sum X	Sum Y	Sum Z	Resultant
Entire Model	N	-441.873	-1.64034	80.4979	449.149

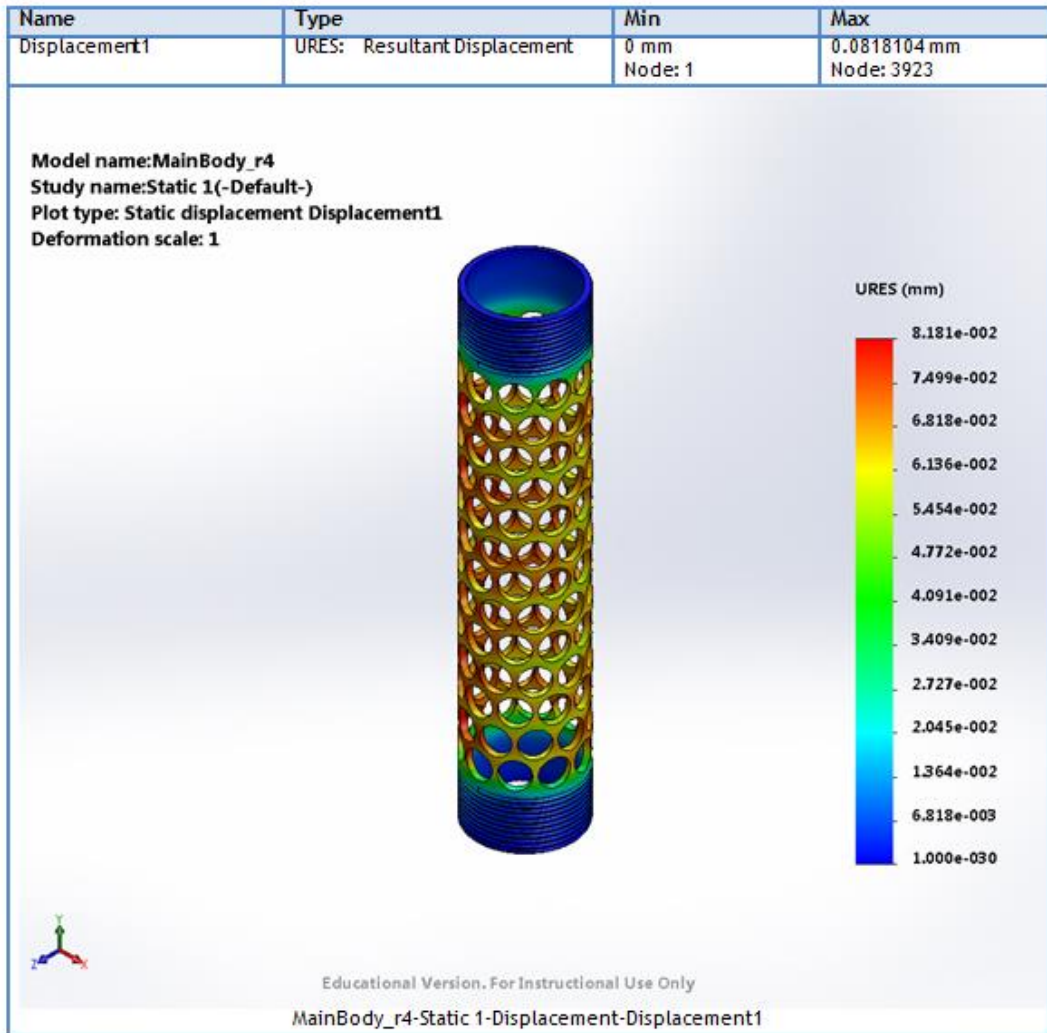
Reaction Moments

Selection set	Units	Sum X	Sum Y	Sum Z	Resultant
Entire Model	<u>N.m</u>	0	0	0	0



Study Results





REFERENCES

- [1] E. Spencer and P. Kovalchik, "Heavy construction equipment noise study using dosimetry and time-motion studies," *Noise Control Engineering Journal*, vol. 55, pp. 408-416, 2007.
- [2] E. Vickers, "Noise Control in Hydraulic Systems," Eden Prairie, MN, 2002.
- [3] N.E. Earnhart, "Modeling and validation of a syntactic foam lining for noise control devices for fluid power systems," PhD Dissertation, G.W.Woodruff School of Mechanical Engineering, Georgia Institute of Technology, Atlanta, GA, 2012.
- [4] AkzoNobel, "Compression of Expancel DE".
- [5] G.F. Harvel. (2015, 10/26/2015). *Temperature Limitations* [Online Web Page].
- [6] J. Hernandez, "GR9 Casting Process," R. Salmon, 2014.
- [7] H. Stevens, "Perforate Sheet Microscopic Image," Georgia Institute of Technology, 2015.
- [8] L.E. Kinsler, A.R. Frey, A.B. Coppens, and J.V. Sanders, *Fundamentals of acoustics*: John Wiley & Sons, Inc. New York, 2000.
- [9] D.A. Bies and C.H. Hansen, *Engineering noise control: theory and practice*: CRC press, 2009.
- [10] McMaster-Carr. Material Costs [Online].
- [11] D.N. Johnston, J.E. Drew, "A technique for the measurement of the transfer matrix characteristics of two-port hydraulic components," *Fluid Power Systems and Technology*, vol. 1, pp. 25-33, 1994.

- [12] I.S.O., "Hydraulic fluid power - Determination of fluid-borne noise characteristics of components and systems " in *Measurement of speed of sound in a fluid in a pipe* vol. ISO-15086-2, Geneva, Switzerland, 2000.
- [13] A.D. Pierce, *Acoustics: an introduction to its physical principles and applications*: Acoustical Society of America Melville, NY, 1991.
- [14] I.S.O., "Hydraulic fluid power - Determination of the fluid-borne noise characteristics of components and systems," in *Measurement of hydraulic impedance* vol. ISO-15086-3, Geneva, Switzerland, 2008.
- [15] R. F. Barron, *Industrial noise control and acoustics*: CRC Press, 2002.
- [16] E. Gruber, R. Salmon, J. McGrael, and K. Cunefare, "Comparison of noise control effectiveness between bladder-style and liner-style hydraulic noise control devices," 2015, pp. 233-240.
- [17] A.P.P. Chemicals, "Expancel Microspheres - A Technical Presentation," ed, 2014.
- [18] K.A. Marek, E.R. Gruber, and K.A. Cunefare, "Linear Multimodal Model for a Pressurized Gas Bladder Style Hydraulic Noise Suppressor," *International Journal of Fluid Power*, vol. 14, pp. 5-16, 2013.
- [19] Wilkes & McLean, "WM3081 Suppressor Drawings," Schaumburg, Illinois.